



Tectonics of Cerberus Fossae unveiled by marsquakes

Simon C. Stähler, Anna Mittelholz, Clément Perrin, Taichi Kawamura,
Doyeon Kim, Martin Knapmeyer, Géraldine Zenhäusern, John Clinton,
Domenico Giardini, Philippe Lognonné, et al.

► To cite this version:

Simon C. Stähler, Anna Mittelholz, Clément Perrin, Taichi Kawamura, Doyeon Kim, et al.. Tectonics of Cerberus Fossae unveiled by marsquakes. *Nature Astronomy*, 2022, 10.1038/s41550-022-01803-y . insu-03868823

HAL Id: insu-03868823

<https://insu.hal.science/insu-03868823>


Submitted on 14 Mar 2023


HAL is a multi-disciplinary open access archive for the deposit and dissemination of scientific research documents, whether they are published or not. The documents may come from teaching and research institutions in France or abroad, or from public or private research centers.

L'archive ouverte pluridisciplinaire **HAL**, est destinée au dépôt et à la diffusion de documents scientifiques de niveau recherche, publiés ou non, émanant des établissements d'enseignement et de recherche français ou étrangers, des laboratoires publics ou privés.

TECTONICS OF CERBERUS FOSSAE UNVEILED BY MARSQUAKES

A PREPRINT


 **Simon C. Stähler**
Institute for Geophysics
ETH Zürich


 **Anna Mittelholz**
Department of Earth and Planetary Sciences
Harvard University


 **Clément Perrin**
LPG-OSUNA
Nantes Université


 **Taichi Kawamura**
Université Paris Cité
Institut de physique du globe de Paris, CNRS
Paris, France

 **Doyeon Kim**
Institute for Geophysics
ETH Zürich


 **Martin Knapmeyer**
Institute for Planetary Science
DLR Berlin

 **Géraldine Zenhäusern**
Institute for Geophysics
ETH Zürich

 **John Clinton**
Institute for Geophysics
ETH Zürich

 **Domenico Giardini**
Institute for Geophysics
ETH Zürich

 **Philippe Lognonné**
Université Paris Cité
Institut de physique du globe de Paris, CNRS

 **W. Bruce Banerdt**
Jet Propulsion Laboratory
California Institute of Technology

June 28, 2022

1 **Keywords** Mars | Tectonics | Volcanism | Marsquakes

ABSTRACT

2 The InSight mission has measured Mars' seismicity since February 2018 and has allowed to investigate
3 tectonics on another planet. Seismic data shows that most of the widely distributed surface faults are
4 not seismically active, and that seismicity is mostly originating from a single graben structure, the
5 Cerberus Fossae. We show that both major families of marsquakes characterized by low and high
6 frequency content, LF and HF events respectively, are located on central and eastern parts of this
7 graben system. LF hypocenters are located at 15-50 km depth and the spectral character suggests a
8 structurally weak, potentially warm source region consistent with recent volcanic activity at those
9 depths. HF marsquakes occur in the brittle, shallow part of the crust and might originate in fault
10 planes associated with the graben flanks. Estimated magnitudes are between 2.8 and 3.8, resulting in
11 a total seismic moment release within Cerberus Fossae of $1.4\text{-}5.6 \times 10^{15}$ Nm/yr, or at least half of the
12 observed value of the entire planet. Our findings confirm that Cerberus Fossae represents a unique
13 tectonic setting shaped by current day volcanic processes, with implications for minimum local heat
14 flow.

15 Introduction

16 Faults are widespread and common on the martian surface [1, 2], providing evidence for brittle deformation throughout
17 the planet's history. Due to the lack of recent widespread volcanism, plate tectonics or high erosion rates which recycle
18 the surfaces of Venus or Earth, martian faults are well preserved over billions of years and do not necessarily correlate
19 with recent tectonic deformation. The InSight mission landed on Mars to observe current day seismicity and thus
20 tectonic activity using a broadband seismometer [3, 4]. Around InSight's landing site [5], wrinkle ridges and lobate
21 scarps, interpreted as buried reverse faults resulting from compression, are widely spread, with clusters in the large
22 Isidis and Hellas impact basins, but also in the planes of Hesperia, Arcadia and Amazonis (Figure 1). Their abundance

was interpreted as the result of secular cooling and associated shrinking of the planet [6], in combination with the weight of the large Tharsis volcanic region 6000 km to the East [7]. Young (<600 Ma), extensional tectonic structures are oriented radial to Tharsis (Figure 13). Westward, these are Cerberus Fossae [8] in Eastern Elysium Planitia, and further southward these are Memnonia and Sirenum Fossae [9]. In conclusion, based on the distribution of young faults one might expect widespread seismic activity north and south-east of the InSight landing site. However, the first seismic data revealed a different picture.

The most significant marsquakes during InSight's first Martian year of operations (observed on Sols 173 and 235 of the mission, thus named *S0173a* and *S0235b*) were located at the approximate distance and in direction of Cerberus Fossae [10, 11]. Analysis of seismic waveforms showed that source mechanisms of the large events from Sols 173 and 235 are consistent with an extensional setting [12], suggestive of ongoing opening of the Cerberus Fossae. Until Sol 1100 (2021/12/31), 18 out of 24 low-frequency (LF) marsquakes for which a location could be determined, have been located at a distance consistent with Cerberus Fossae [13, 14] and for seven of those, a focal mechanism could be determined, generally extensional [15]. LF quakes are similar in character to earthquakes, with clear P- and S-waves, and they are thought to occur in the lower crust or uppermost mantle [11], between 15 and 50 km depth [12, 16]. A second class of marsquakes is termed high-frequency (HF) events, due to significant signal energy above 2 Hz [13]. A long signal duration is interpreted as the result of a shallow hypocenter of less than a few km depth, which excites reverberations of seismic waves in shallow subsurface layers [17]. HF events have been detected in much larger numbers, 1150 until 2021/12/31, yet they have smaller magnitudes than LF events; their distance is clustered around 1500 km, and due to a lack of clear polarisation, their direction as seen from the lander has not been determined. Thus no tectonic explanation has been provided for this most common type of Martian seismicity yet. Here, we determine the direction of HF events and corroborate the unique tectonic setting of the Cerberus Fossae System. We investigate the source character of LF events which indicate a warm source region at depth as opposed to the brittle and shallow source region of HF events. Combining all information from both event classes allows to derive a consistent picture of the tectonics in the Cerberus Fossae system.

So far, no other tectonic feature on the InSight hemisphere of Mars has been unequivocally confirmed to be seismically active [13], and only recently, on Sol 976 (2021/09/01), InSight detected large marsquakes on the far side, in the Southern Tharsis province [18]. Since no marsquakes at all have been clearly localized on wrinkle ridges or lobate scarps, i.e. contractional features, Cerberus Fossae offers unique insight into Mars' tectonics as a whole.

Geological context

The Cerberus Fossae system is approximately 1200-2300 km (20-40°) east of the InSight lander (Figure 2b,c). It has been described as a dike-induced graben system [19], or a system of collapsed and widened volcanic fissures [20, 21]; we will refer to it as a system of fossae, which is the descriptive term for elongated fractures on Mars. Cerberus Fossae consists of five main graben features (G1-G5 in Figure 2b) trending NW to SE and between 250 and 600 km long, but further segmented. Smallest segments that can be identified on the surface are 5-10 km long [19]. The westernmost fossae are more mature (i.e., larger width and throw) and well connected, as opposed to the hardly connected segments at the eastern fossae [19]. Cerberus Fossae was previously identified as the location with most recent volcanic activity on Mars [2] dated to less than 10 Ma [22], contemporary with the deposition of surficial basalt deposits over Eastern Elysium Planitia [8, 23]. Moreover, [24] identified symmetric dust deposits in the central part of the fossae, the Cerberus Mantling Unit (CMU; Figure 2d), and hypothesized that those are pyroclastic deposits younger than 200 ka. Large-scale radially extensional and concentric contractional faulting (global fault map in Figure 13) from the topographic load of the Tharsis volcanic province would create the extensional stress field in North-west direction in Eastern Elysium Planitia [7, 25]. The actual fracturing in the specific location could be due to weakening of the crust due to partial melting below Elysium Mons and a dike system extending from there [26, 27].

Marsquake Hypocenter Locations

Figure 1 shows the combined probability density of all LF quake locations including distance and direction using recently obtained back azimuth estimates [28] and velocity models [29], and it peaks at Cerberus Fossae. The uncertainty on back-azimuth results in a relatively large geographical spread in North-South direction. But given that the distance spread (in East-West direction) of the observed marsquake cluster is small, it can a priori be assumed that their N/S spread is of similar magnitude, allowing to place all of these events into Cerberus Fossae. The five segments of the Cerberus Fossae grabens (G1-G5) are concentrated in two main regions [19], where G1, G2, G3 are in a distance range of 18° – 27° from InSight, while G4 spans the range of 33° – 39°. G5 is more faint, less mature and bridges the two main regions. The graben strike is 15° off the direction of the lander. Distance differences of LF events can most easily be explained by different locations along the fossae. To identify such locations, we evaluate if the event cluster is

consistent with certain locations along the fossae (Figure 2a,b) when varying the seismic velocity models. In the "near" end-member model, the cluster of events would occur at the eastern end of G1 or in G5. In the "far" case, it would be placed on G5 and G4. In any case, the dominant location of marsquakes at the eastern end of the western section is compatible with the observation of east-ward decreasing maturity, that would imply increased stress concentrations at the propagating fossae [19]. A single event, S0325a [13] would be located at the eastern end of G4 (not shown in Figure 1), but given that this event has a poorly determined back azimuth [28], it cannot be clearly attributed to Cerberus Fossae. We conclude that the majority of *localized* LF events on the InSight hemisphere cluster in central Cerberus Fossae (Figure 1).

Localising HF events has not been attempted at all so far due to the strong scattering and the lack of ballistic arrivals [17]. We realign the events to better constrain relative distances and stack horizontal component envelopes. We find a surplus of energy in $78 \pm 12^\circ$ backazimuth around the P-wave arrival, consistent with a source in direction of Cerberus Fossae (see Supplement). We further examine their distance distribution and while it is broader c.f. LF events, we find that it indeed matches the extent of Cerberus Fossae (Figure 1 and 2a). Thus, we can plausibly assume that shallow HF seismicity also originates in Cerberus Fossae. The HF sources are spread over a large part of the Fossae, as opposed to the more focused distribution of deeper LF events.

Seismic Moment

Estimating Seismic Moment Release

MQS routinely estimates magnitudes [30] and their uncertainties. For LF events, the magnitude uncertainty takes into account the distance uncertainty as well as the error in estimating the long-period amplitude [30]. Identification of marsquakes is limited to times of low wind at InSight, which make up approximately one third of the total duration averaged over the mission [13, 31]. When estimating the total seismic activity rate of a region, one needs to take into account not only the detection probability due to wind noise, but also the inherent randomness of number of events per year. [32] propose a Markov Chain Monte Carlo method to estimate the likelihood for annual moment release and maximum event size, given a short and incomplete catalog. Following this procedure, we estimate the total annual moment rate in Cerberus Fossae as $1.4\text{--}5.6 \times 10^{15}$ Nm/yr (SM A.3). Regarding Mars' seismicity as a whole, SEIS observed a total of 39 LF marsquakes on the InSight hemisphere rated as quality A,B or C (A-D is highest to lowest, where D is unlocatable) by MQS up to December 31, 2021 [14]. Five of them are unequivocally located outside Cerberus Fossae, compared to 14 in Cerberus Fossae. The remaining 20 cannot be located due to noise. Thus, from the observations so far, the small region of central Cerberus Fossae accounts for at least half of the seismic moment release of the whole InSight hemisphere.

Seismic vs Geological Deformation

Following the morphological estimate of [22], the formation of the Cerberus Fossae grabens G1-G4 requires deformation equivalent to a seismic moment, $M_{0,\text{total}} = 2.1 \pm 0.5 \times 10^{24}$ Nm, assuming a constant rate \dot{M}_0 since initiation of the spreading 5-20 Ma ago, $\dot{M}_0 = 0.5 - 2.2 \times 10^{17}$ Nm/yr. This prediction exceeds our seismic observation by a factor of 50 and is a first indication that the current seismicity rate is not representative for the entire formation process.

Next, we focus on the observed seismicity cluster which spreads over 400 km distance and a range of ~ 20 km in depth (thus providing an area A). Using a shear modulus of $\mu = 24$ GPa [33] and assuming that all of the seismicity was extensional, the observation is equivalent to a slip rate of $\dot{s}_{\text{seism}} = \frac{\dot{M}_0}{\mu A} = 7 - 30 \times 10^{-6}$ m/yr. For G1 and G2, the geological deformation rate is $\dot{d}_{\text{geol}} = 5 - 73 \times 10^{-5}$ m/yr [34]. The central young CMU (53-210 ka [24]) shows a throw of at least 100 m, equivalent to a slip rate of $\dot{s}_{\text{geol}} = 5 - 20 \times 10^{-4}$ m/yr over the last few 10 ka. We therefore conclude that the current seismic slip rate \dot{s}_{seism} explains only 1 - 10% of the total deformation, \dot{d}_{geol} , preserved in the geological record.

The shallow seismicity associated with the HF events is at least a factor of 10 below the LF events due to their smaller magnitudes and it is distributed over a larger area. It can therefore not explain the discrepancy between geological deformation and observed seismicity.

A Case for Dike-induced Tectonic Activity in the Source Region

Spectral Characteristics

The duration of a quake, whether on Earth or Mars, places a limit on the coherent high-frequency seismic energy radiated from it. This is typically expressed via the corner frequency in the source spectrum, f_c , above which displacement amplitude, $A(f)$, decreases as f^n , where $2 < n < 3$ [35]. For all investigated LF events in Cerberus Fossae, we find that $0.45 < f_c < 0.95$ Hz. As shown in Figure 4c, this is significantly less than the values found empirically for $M_W \approx 3$ earthquakes [36, 37], which is 2-10 Hz. In comparison, LF marsquakes outside Cerberus Fossae, specifically a recent marsquake in Syrtis Major Planum, S1102a (2022/01/02, Fig 4b), but also other events at distances of 3000-4000 km (red stars in Fig 4c) show significantly higher values of $f_c > 1.5$ Hz. The corner frequency of the shallow HF events is significantly higher (see figure 4b). For the largest HF events, a roll-off in displacement spectrum is observed above 3 Hz, which puts a lower limit on the f_c , given the unknown attenuation of the upper crust. While their magnitudes range from $1.5 < M_W < 2.5$, this f_c is still at the low end of terrestrial quakes, although it must be noted that their absolute magnitude is uncertain due to the complicated propagation mechanism.

A feasible explanation for the observation of "slow" quakes is a significantly reduced shear wave velocity, β , in the source region, because in classic models f_c scales linearly with β [35], i.e.,

$$f_c \propto \beta^3 \sqrt{\Delta\sigma/M_0}. \quad (1)$$

where $\Delta\sigma$ is the stress drop. InSight observed low β of 1.3-1.8 km/s in the uppermost ten km below the lander as derived using receiver functions [10, 33] and autocorrelations [38], which is a factor of ~ 2 below the value in terrestrial crustal models [e.g. 39]. If the hypocenters were located within this layer, this could explain a factor of 2 in corner frequency compared to the bulk of terrestrial crustal earthquakes, but hardly the observed 5-10. Also, so far all published results agree on LF event depths of at least 15 km [12, 16, 40, 41], where β is comparable to terrestrial values.

Local weakening, e.g. due to warmer materials nearby a dike in the source region, could present a second effect leading to the observations. The stress drop ($\Delta\sigma$ in eq. 1) describes the difference of the shear stress on the fault plane before and after the quake. It can be derived analytically for simple fault geometries in homogeneous media, and otherwise represents an empirical term [42]. As a general rule, low values for f_c and thus $\Delta\sigma$ are found in volcanic settings, where material is heated and close to ductile behaviour [43]. This would require the hypocenters to be located in a zone of increased temperature, possibly close to a magma chamber feeding shallower dikes (Figure 5). This explanation is consistent with the depth estimates for LF and HF events. The deep LF events are closer to the weakening heat sources and thus show a slower rupture process than the more shallow and fast, brittle HF events.

A third possible explanation would be that the lower gravity on Mars will reduce yield strength and could thus lead to generally lower stress drops and therefore f_c . However, this general trend is not seen on Earth, e.g. when comparing earthquakes at different depths [44], and shallow moonquakes show even higher f_c values [45]. Finally, as stated above, large marsquakes outside of Cerberus Fossae have significantly higher corner frequencies, which fall within the range expected for terrestrial quakes of similar size (red line in Figure 4b). This observation confirms that Cerberus Fossae events are different and, combined with the very frequent and localized observations of quakes from this source region, highlights the unique setting of Cerberus Fossae.

Recent Volcanism in Cerberus Fossae

The CMU near Zunil crater has been hypothesized as a recent product of explosive volcanism [24], based on the symmetric distribution of dust and streaking of secondary craters away from the structure (Figure 2d). The dust and streaking directions overlay that of Zunil crater itself, dated at 0.1-1 Ma. While the hypothesis of explosive volcanism may be unproven, the detailed age estimates of the CMU of 53-210 ka, make it one of the youngest features mapped on the Martian surface to date [24]. Because there is no sign of younger volcanism locally, the structure would have to be considered dormant or inactive.

Terrestrial volcanoes of this age can still be in an active state with ongoing fluid motion identified by seismic activity [46]. The observation of marsquakes around the CMU is thus intriguing and we compare our observations with two categories of seismic activity near dormant volcanoes on Earth (for an overview, see e.g. [47]): (1) Deep low frequency events (DLEs), which are "slow" quakes of magnitudes < 2 . These events typically occur in swarms, i.e. week- to year-long activity bursts. (2) Volcanic tremor, long-duration, monochromatic signals.

In comparison, our studied events on Mars do not quite match any of these two categories. While martian LF events are abnormally slow, they do not qualify as DLEs, because they are too large in magnitude (which would require very significant subsurface magma motion). Moreover, their recurrence rate also shows no deviation from a stationary Poisson process (SM A.3), unlike DLEs, which occur in swarms. We note that at distances of 1500 km or more, the

VBB seismometer lacks the resolution to observe very slow events, including DLEs below magnitude 2.5 (region below the red line in Figure 4). We therefore cannot rule out signals from fluid motion, but discussed event observations are not consistent with Earth-like DLEs. Others [48] investigated whether several LF marsquakes could be explained by volcanic tremor, but found that for the magnitude and spectral content, very large magma flow rates over short time windows would be needed. This is in apparent contradiction to the low number of marsquakes observed so far and the lack of surficial expressions of current active volcanism. Also, the events discussed in this study show very clear P- and S-arrivals, unlike the more emergent signals of tremor on Earth. In summary, we do not find evidence of tremor or generally fluid motion in the seismic data.

Inferred Rupture Size

Lastly, under the assumption of a circular source, f_c allows to infer the source radius as $r = 0.38 \frac{\beta}{f_c}$ [49]. Within the range of β between 2-3 km/s, we obtain rupture plane radii of 1200–1800 m. This is below the minimum size of mapped surface segments within the Cerberus Fossae grabens (5-10 km [19]), suggesting that small to moderate size marsquakes are not primarily limited by fracture geometry and that over longer observation times, significantly larger marsquakes occur, compatible with the large, potentially co-seismic boulder avalanche traces observed in orbital imaging [50]. The shallower HF quakes likely happen in the uppermost, low- β layer [33], with source radii between 150 and 300 m.

Discussion: The Evolution of Cerberus Fossae

Seismic data confirm ongoing opening of the Cerberus Fossae on Mars. Seismicity at 15-50 km depth with slow rupture processes suggests an extensional stress regime located in a warm source region. If the seismicity of the central event cluster is related to the CMU, the observed seismic strain rate is far too low for a constant, slow opening of the fractures. This is consistent with rapid creation in a volcanic eruption 53-210 ka ago, as observed for dike-induced fractures on Earth [51].

The east-west distribution of our events shows focused seismic activity in the center of Cerberus Fossae with generally low current seismicity compared to inferences from the geological record. This indicates that the opening rate of the grabens has not been constant. Instead, most of them likely opened rapidly and became mostly passive after a short time. The seismic observation period is short and our data merely represent a snapshot of the overall seismicity of Cerberus Fossae. Nevertheless, the fact that we do not see LF seismicity in most parts of Cerberus Fossae, specifically in the fractured western part where the largest deformation can be found, suggests a dynamic process that ceases after an initially active phase and continues to propagate eastward.

We propose that the shallow seismicity from HF events is created by ruptures at shallow depth due to the graben structure itself, possibly the subsurface continuation of the graben flanks (Figure 5). The rapid rupture associated with these quakes is not consistent with sources such as landslides or other mass wasting processes. More likely it is caused by the release of residual stress. A modulation of the HF quake rate with a period of one Martian year was found [31] and its phase matches the peak solar elevation in equatorial latitudes. Given that significant parts of Cerberus Fossae are deep enough to be in shadow over half of a Martian year, this is a plausible correlation and consistent with shallow sources. However, a physical model connecting the two factors, illumination and quake rate, is still missing.

Globally, the clearly localized seismicity suggests that global contraction and therefore lithospheric compression are not the dominant driver of contemporary tectonics on Mars. Cerberus Fossae alone releases $1.4\text{--}5.6 \times 10^{15}$ Nm/yr seismic moment, a factor of 2-8 more than the Moon globally [32], where shallow seismicity has been identified on compressional faults [52]. The slow character of the Cerberus Fossae events requires a warm source region. To be close to ductile rheology, a temperature of 1000 ± 100 K is required for basaltic compositions [53, 54]. Assuming a quake depth of 40 ± 10 km, this results in a local crustal thermal gradient $\Delta T/\Delta z = 20 \pm 2$ K/km in Cerberus Fossae and a local heat flow of 36 ± 10 mW/m² (assuming thermal properties of basalt [55]), a factor of 1.7 above the global average values of 21 ± 7 mW/m² and 22 ± 1 mW/m² found by joint seismic and geophysical inversions [41, 56]. Such a localized high heat flow in Elysium has strong geodynamical implications for the crustal thickness of the whole planet, namely, it is difficult to reconcile with a thicker crust in the Southern hemisphere [27].

The distribution and character of marsquakes show that the global stress field cannot exclusively explain the origin of Cerberus Fossae. Instead, partial melting below Elysium likely weakens the crust locally and allows the grabens of Cerberus Fossae to open. Across the solar system, a pattern emerges, where the present-day tectonics of the larger terrestrial planets - Mars, Venus, and the Earth - is dominated by internal dynamics [57] instead of purely passive cooling and shrinking, as it is found on the smaller Moon and Mercury.

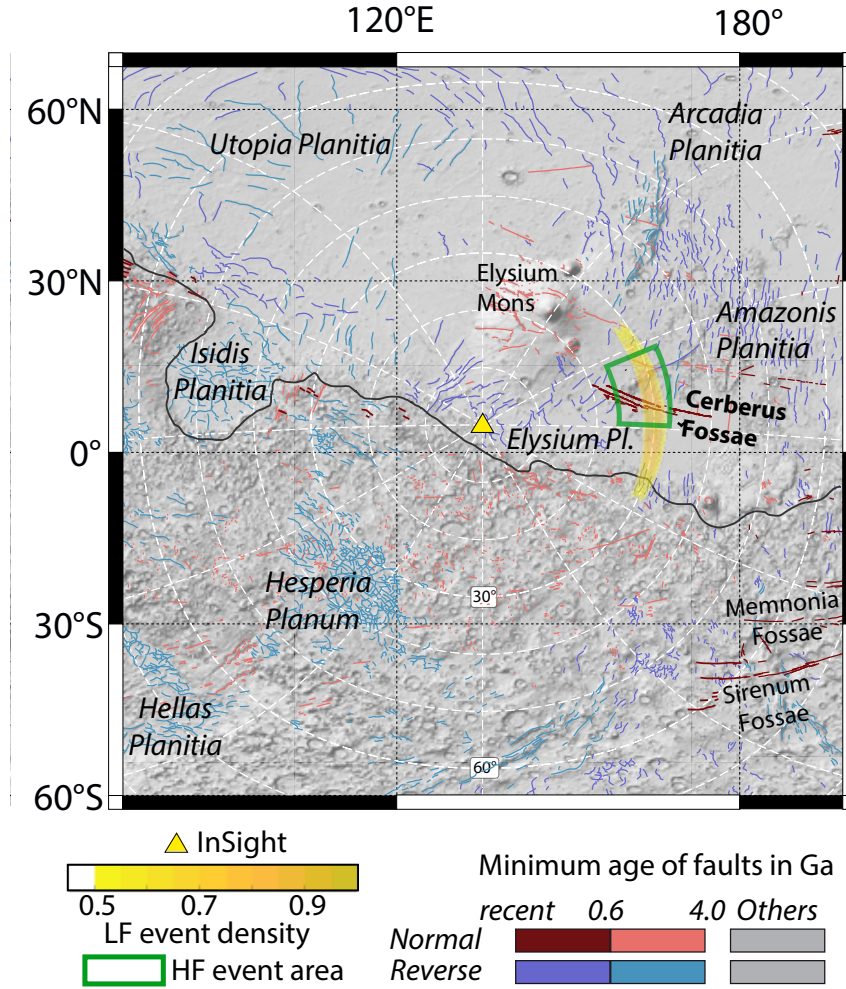


Figure 1: Faults and major geographic features around the InSight landing site [1, 19] color-coded by age. The yellow shaded area marks the normalized density of low frequency (LF) quakes [14, 28]. The green box highlights the backazimuth range found by our analysis for HF marsquakes, corresponding to the dashed line in figure 3 and the distance range in which 80% of seismicity is present. Background shading: MOLA topographic map [58]. A global version of this map is available in the supplement (fig. 13)

Acknowledgements

We acknowledge NASA, CNES, partner agencies and institutions (UKSA, SSO, DLR, JPL, IGP-CNRS, ETHZ, IC, and MPS-MPG), and the operators of JPL, SISMOC, MSDS, IRIS-DMC, and PDS for providing SEED SEIS data. S.C.S. acknowledges funding from ETH research grant ETH-10 17-3. S.C.S., G.Z., and D.G. acknowledge support from ETHZ through the ETH+ funding scheme (ETH+2 19-1: “Planet MARS”). A.M. acknowledges support from ETH 19-2 FEL-34 and the Harvard Daly Postdoctoral Fellowship. C.P. acknowledges support from CNES as well as Agence Nationale de la Recherche (ANR-14-CE36-0012-02 and ANR-19-CE31-0008-08). W.B.B. was supported by the NASA InSight mission and funds from the Jet Propulsion Laboratory, California Institute of Technology, under a contract with the National Aeronautics and Space Administration (80NM0018D0004). This is InSight contribution 233.

1 Tables

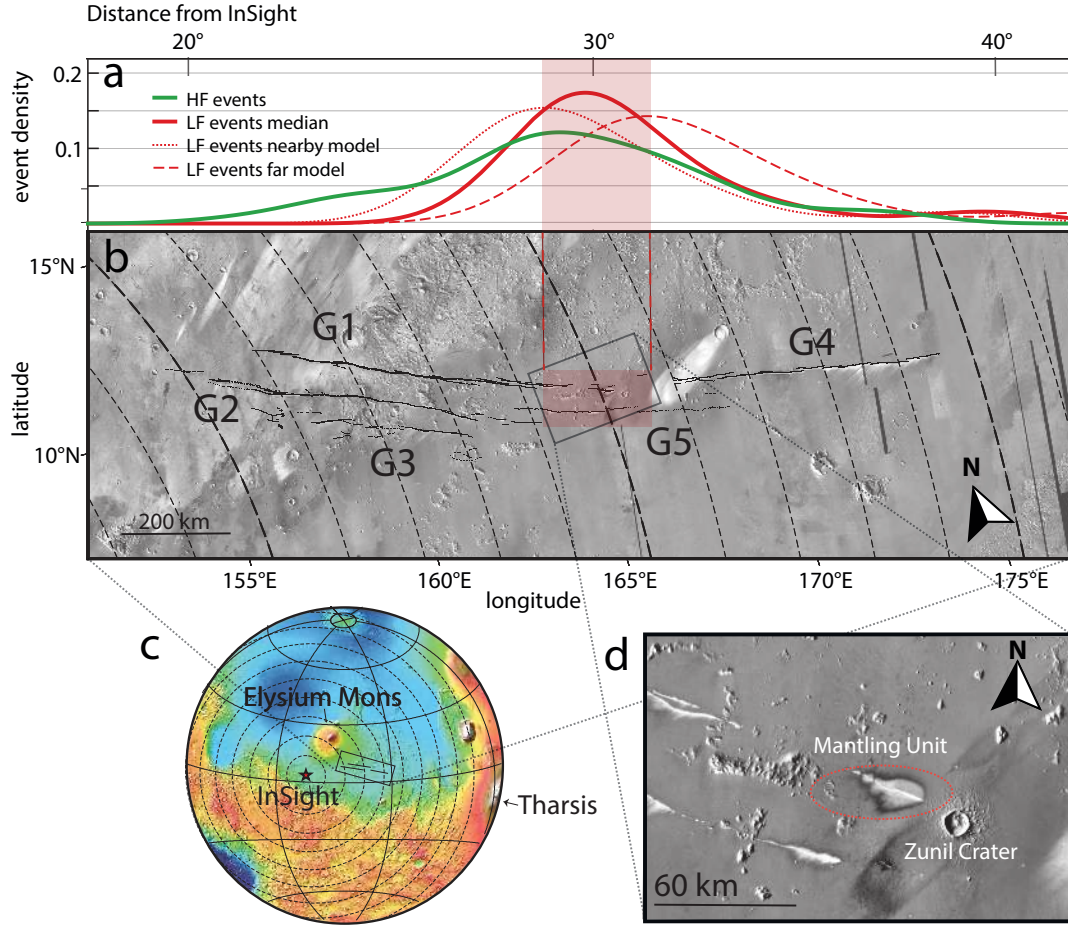


Figure 2: (a) Density of seismic moment release along the profile of Cerberus Fossae. Probability density functions (PDF) from a Gaussian kernel density estimation of high frequency (HF; green) and low frequency (LF; red) moment are shown separately. For the LF events, 3 candidate distributions based on different mantle models are shown ("median" model is shown in Figure 1). The red box highlights the area between near and far model peaks in (a) for easier comparison with (b). (b) Oblique Mercator projection of Mars Odyssey's Thermal Emission Imaging System (THEMIS; day-time infrared) highlighting the 5 main graben features G1-G5 of Cerberus Fossae (mapping from [19]). (c) MOLA topography inset for global context and 10 degree distance circles around InSight. (d) The area of highest marsquake density: The Cerberus Mantling unit recently identified as a volcanically active feature by [24] is circled.

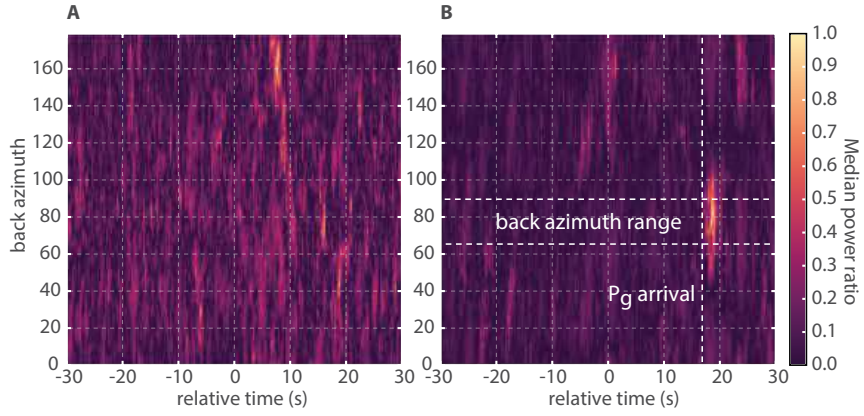


Figure 3: Energy ratio between radial and transversal horizontal component for HF envelope stack (a) before and (b) after re-alignment (see A.2). The energy maximum at a backazimuth of $78 \pm 12^\circ$ (dashed lines) corresponds to P-wave energy from the central part of Cerberus Fossae. The time axis is relative to an arbitrary offset used before alignment, the P_g -arrival is thus marked.

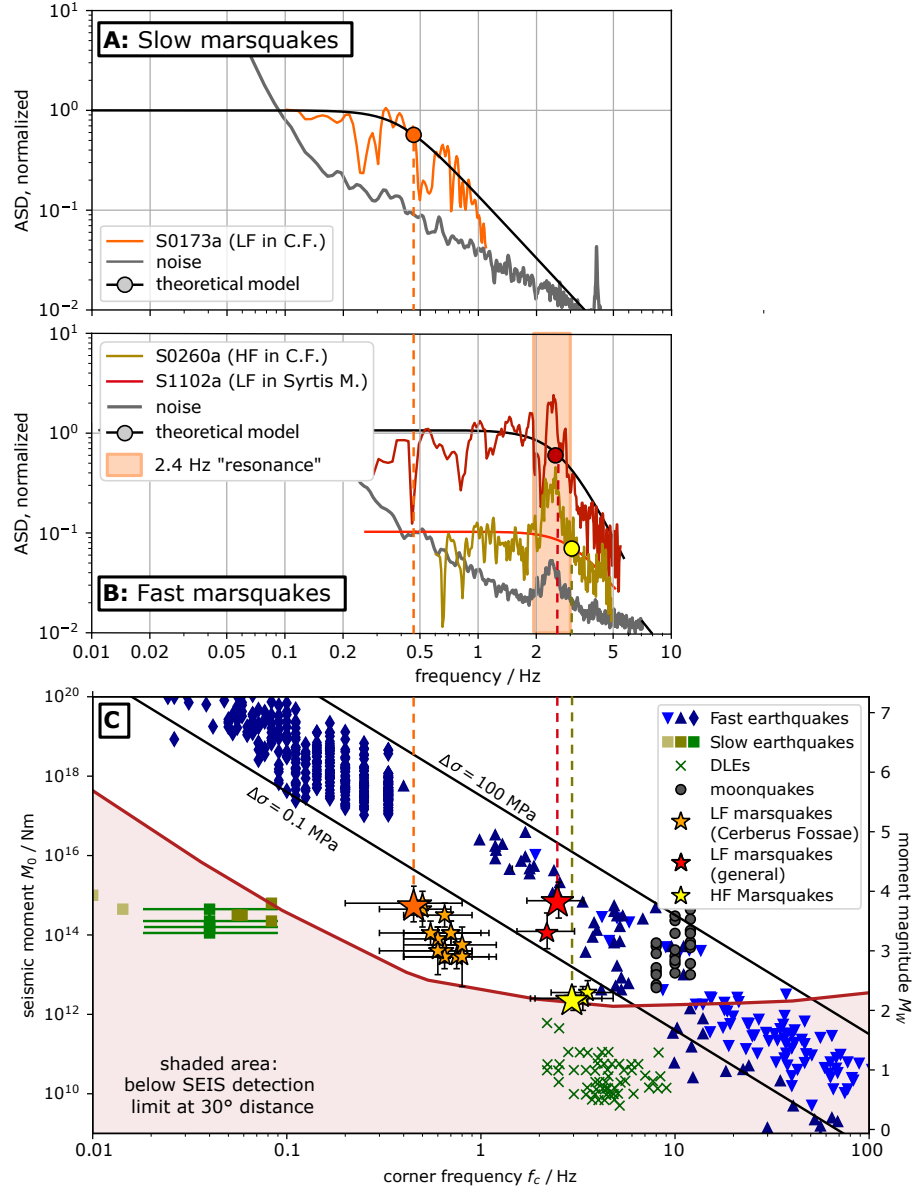


Figure 4: Spectra of marsquakes and source parameters compared to terrestrial and lunar quakes. (A): Source spectra of Cerberus Fossae low frequency (LF) marsquakes S0173a. (B): Source spectrum for high frequency (HF) marsquake S0260a and distant LF marsquake S1102a. The source spectra were estimated from the vertical component for the P-wave window, normalized and corrected for attenuation, assuming $Q_\mu = 1000$, to match P- and S-falloff. The black solid lines show best fitting theoretical source spectra using a Brune model with exponent $n = 2$ or 3 , circles are modelled corner frequencies. The background noise curves in (A) and (B) are from data before the P-wave arrival. The orange area in (B) is the local "2.4 Hz" subsurface resonance described in [59, 60]. (C): Seismic moment M_0 vs corner frequency f_c for different types of quakes observed on the Earth, the Moon and Mars. Blue symbols mark regular, "fast" earthquakes, following a cube law between seismic moment and corner frequency for 3 datasets of shallow earthquakes (in order of symbols: [36, 61, 62]). The brown squares mark a group of deep, slow events in Japan [63], the green crosses mark slow events related to volcanism, observed in Germany [46]; gray dots are fast shallow moonquakes [45]. Black lines are f_c values for stress drops of 0.1 and 100 MPa for $\beta = 3$ km/s. HF marsquakes (yellow stars), as well as LF marsquakes outside Cerberus Fossae (red star) follow the $f_c \propto M^{-3}$ trend of earthquakes, while Cerberus Fossae LF events are significantly slower.

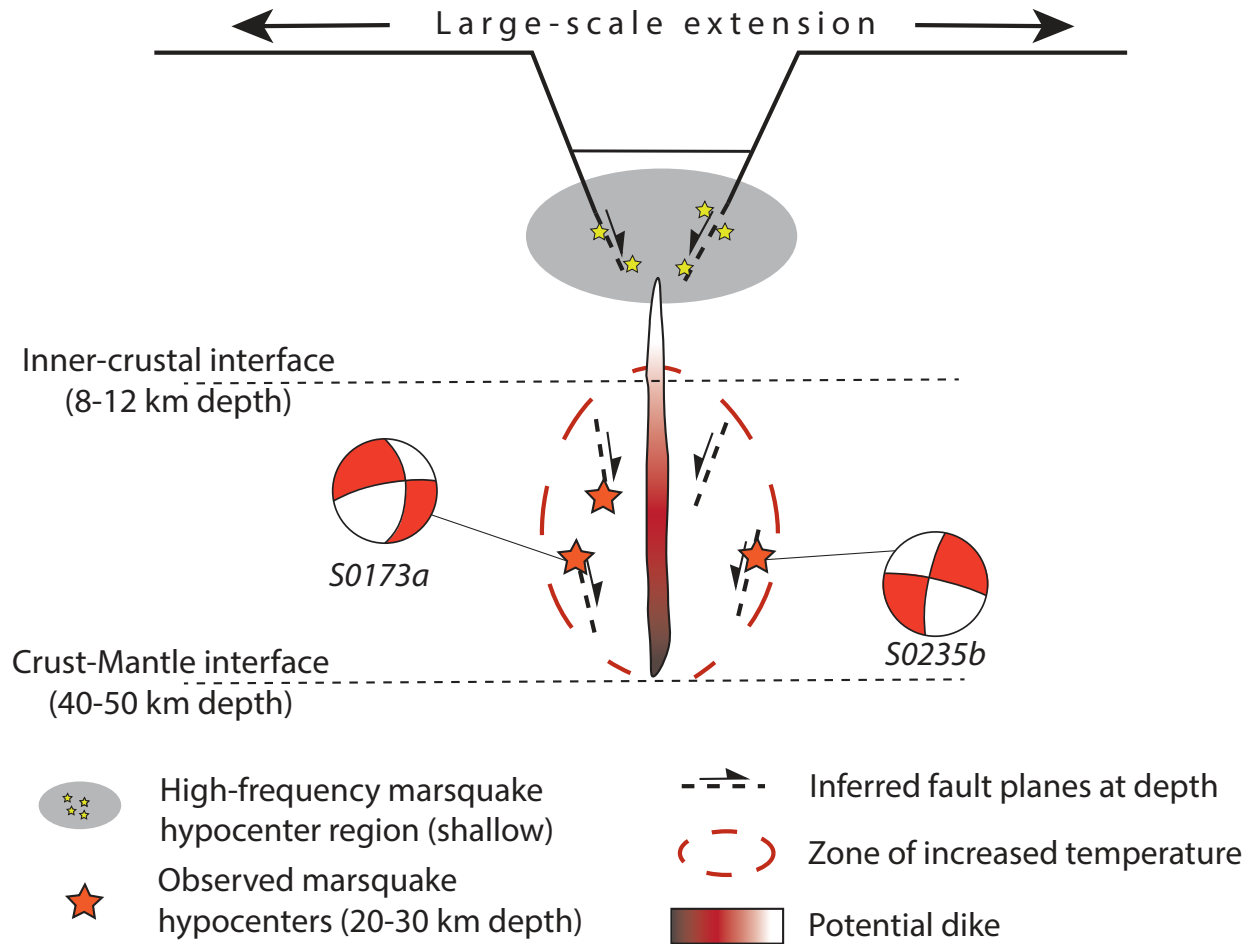


Figure 5: Sketch of an active part of Cerberus Fossae viewed from East. The low frequency marsquake depths indicate faulting in the lower part of the crust, the low stress drop suggests that hypocenters (red stars) are located in the zone of increased temperature (red dashed) around a (recently) active dike at depth. Event S0235b has been previously located to the North of the fault, S0173a to the South. In combination with the focal mechanisms inferred in [12], rupture planes dipping towards the dike are plausible. In the shallow part, high frequency marsquakes are caused by residual stress on the flanks of the graben (yellow stars). The focal mechanisms are plot as seen from 70°azimuth.

Event	Quality	Distance [deg]	M_W	f_c	Back Azimuth [deg]			
					MQS	Uncertainty	Pol.-based	Uncertainty
Events in Cerberus Fossae								
S0173a	A	30.0	3.7 ± 0.3	0.45 ± 0.15	91	79-102	88	78-103
S0235b	A	28.7	3.7 ± 0.2	0.45 ± 0.15	74	66-88	77	64-100
S0802a	B	30.0	2.9 ± 0.2	0.75 ± 0.25	-	-	82	65-96
S0809a	A	29.8	3.3 ± 0.2	0.7 ± 0.3	87	67-105	91	82-100
S0820a	A	30.2	3.3 ± 0.2	0.55 ± 0.25	88	76-107	106	85-120
S0864a	A	28.7	3.1 ± 0.2	0.6 ± 0.2	97	83-116	90	66-110
S0916d	B	29.3	2.9 ± 0.2	0.95 ± 0.35	-	-	97	41-114
S1133c.	A	30.2	3.8 ± 0.2	0.8 ± 0.2	-	-	90	70-110
Events likely in Cerberus Fossae								
<i>S0105a</i>	C	32.5	3.0 ± 0.4	0.5 ± 0.2	-	-	112	95-133
<i>S0325a</i>	B	39.7	3.7 ± 0.3	0.5 ± 0.2	-	-	57	43-73
<i>S0407a</i>	B	29.3	2.9 ± 0.3	0.7 ± 0.2	-	-	57	43-169
<i>S0409d</i>	B	31.1	3.2 ± 0.3	0.5 ± 0.2	-	-	70	50-90
<i>S0474a</i>	C	29.1	2.9 ± 0.3	0.6 ± 0.2	-	-	97	72-123
<i>S0484b</i>	B	31.8	2.9 ± 0.2	0.6 ± 0.3	-	-	100	80-120
<i>S0784a</i>	B	34.5	3.3 ± 0.2	0.8 ± 0.3	-	-	115	92-136
Other marsquakes								
S1102a	A	74	3.6 ± 0.2	2.85 ± 1.0	286	261-309	22	354-55
S0185a	B	59.8	3.1 ± 0.3	1.8 ± 0.6	-	-	-	-

Table 1: Table summarising marsquake parameters. The marsquake events, type (BB = broad-band, LF = low-frequency), distance, M_W , quality (highest to lowest for A, B, C) and MQS back-azimuths are taken from the MQS catalog [14]. MQS uncertainties are described in [13]. Magnitude M_W based on [30]. Polarization back-azimuth values and uncertainties are described in [28]. Events in *italics* have less certain back-azimuth estimates (see [28]).

2 Methods

Distance

Marsquakes are located by the Marsquake Service (MQS; [64]). Their respective distances from the InSight lander are determined from seismic data in combination with geophysically constrained velocity models, i.e. without taking prior tectonic information into account. For LF events, MQS uses the arrival time difference between P- and S-waves, the two strongest seismic body waves to compute the distance of the event from InSight. This travel time difference is compared to predicted travel times for a suite of inferred one-dimensional velocity-density structure models of Mars' interior [13, 16, 56]. The uncertainty in absolute distance is a combination of uncertainty in picking the arrival times and the span of possible seismic velocities in the interior model suite [65]. The uncertainty in seismic velocities from most recent interior models is about 5% [56]. If one separates the effect of pick uncertainty and velocity model uncertainty, the relative distances of all marsquakes can be determined with much higher precision than their absolute distances, allowing to identify a cluster of seismic activity. The absolute distance of this cluster can then be estimated using different types of interior velocity models (Figure 2a).

We use P and S-wave pick times of the MQS catalog version 9 [14] for marsquakes in distances within 3000 km ($\approx 50^\circ$) of InSight and investigate the distance spread resulting from 2 end member velocity models and one median model from [29]. The model with slowest/fastest velocities creates the set of *nearby/far* solutions. From these event distances, we determine a normalized seismicity density over distance (Figure 2a; see A.1). The uncertainty in depth of the events is estimated to be on the order of 20 km, and is reflected in the distance distributions.

For HF events, we use MQS S/P picks (termed S_g and P_g , due to crustal propagation [13]) and according to MQS practice we assume that the onsets of the two observed phases propagate with velocities of $v_{Pg}=4$ km/s and $v_{Pg}/v_{Sg} = \sqrt{3}$ [13], consistent with velocities of the lower crust [33]. The 286 HF events are spread over a distance range from 1200-2500 km (20 to 40°), with a clear maximum between 1700 and 2000 km (27 and 32° ; see Figure 2a), consistent with the center of Cerberus Fossae (Figure 2a).

Direction

Because InSight comprises a single-station global network, the direction towards an LF event (termed back-azimuth) is estimated independently from the distance. MQS originally uses the linearity of P-wave motion [65], which only resulted in direction estimates for 8 events, due to the low SNR. A recently proposed more robust alternative is based on the eigenvalues of the spectral matrix [66] for P- and S-waves [28]. With this approach, we found that at least 14 events are located within 150 km north/south of Cerberus Fossae as seen from InSight (see table 1). By application of the method to well-located terrestrial data of similar signal-to-noise ratio, [28] found that this is within the uncertainty of the method at a distance of 1500 km. Therefore, all these 14 LF marsquakes are compatible with locations in Cerberus Fossae (Table 1).

The direction of HF events has so far been unknown, because the highly scattered first arrival has not shown an increased degree of polarization for any single event [13, 28]. Here, we make use of the large number of HF events observed so far. To investigate whether the epicenters of the HF events are in a similar location, we stack all HF event waveforms and compare horizontal seismogram power in the radial direction of central Cerberus Fossae (70° from North, radial) with that in the orthogonal direction (transverse). If the sources are indeed located in this direction, we expect the P-wave arrival to show higher energy in radial direction, at least in a short time window, in which ballistic waves dominate. Figure 3a shows no clear effect, likely due to time shifts between the phase arrivals of individual events. We follow [67] and conduct a realignment of the P_g arrivals using a multichannel cross-correlation method [68]. After alignment, we select 32 events in a distance between 23° and 25° to minimize the variation in backazimuth within the event stack. We find that the ratio of radial to transverse energy is maximized for a back-azimuth of $78^\circ \pm 12^\circ$, supporting the identification of Cerberus Fossae as source region of the HF events (see A.2).

Spectral character

Estimating the source spectrum of a quake is difficult from a single seismic record, because the high-frequency fall-off is affected by attenuation, both from intrinsic viscoelasticity, Q_i [69, 70], as well as scattering, Q_{scat} [71]. For frequencies above 1 Hz, scattering has been found to affect P- and S-waves considerably, on Earth [72] and on the Moon [73]. Below 1 Hz, both attenuation mechanisms affect S-waves significantly stronger than P-waves due to longer propagation time of S-waves. From a single seismic record, one can isolate source effects by correcting the observed spectra for different values of intrinsic shear wave attenuation $Q_i = Q_\mu$ until the P- and S-spectra match. Doing that, we find that the P- and S-wave spectra of LF events cannot be explained by effects of intrinsic attenuation alone, but show a strong

source imprint. As an example, Figure 4a shows the P-wave spectrum of the high-SNR event S0173a corrected for an average $Q_\mu = 1000$, requiring a corner frequency $f_c = 0.45 \pm 0.15$ Hz.

Following [35, 74], we assume that the source spectrum of a marsquake can be described by

$$A_{\text{src}}(f) = \frac{\Omega_0}{[1 + (f/f_c)^{2n}]^{1/\gamma}}, \quad (2)$$

where Ω_0 is the amplitude at long-period, describing the total deformation caused by the event. In the classical definition of Brune, [35], $\gamma = 1, n = 2$. This fits the theoretical prediction of the Haskell source model of a single patch rupturing from one side to the other, while elongated faults lead to values of $n > 2$. The corner frequency f_c is related to the stress drop $\Delta\sigma$ by

$$f_c = k\beta \sqrt[3]{\frac{16}{7} \frac{\Delta\sigma}{M_0}}, \quad (3)$$

where β is the shear wave speed, M_0 the scalar moment of the source and k a dimensionless scaling parameter. For circular ruptures, [75] showed that $k = 0.38, 0.26$ for P- and S-waves, respectively. All else being equal, we therefore expect the P- and S-wave spectrum to be similar, with a corner frequency that is potentially higher for the P-wave.

The measured displacement spectrum at the receiver $A(f)$ is further shaped by viscoelastic attenuation along the path, described by the intrinsic quality factor $Q(f)$

$$A(f) = A_{\text{src}}(f) \cdot \exp\left(-\pi \frac{fT}{Q(f)}\right) \underset{Q(f)=Q_0}{=} A_{\text{src}}(f) \cdot \exp(-\pi ft^*), \quad (4)$$

where T is the propagation time. Q generally depends on frequency, often expressed as $Q(f) = Q_0 f^\alpha$ with $\alpha \approx 0.2$ [76]. Over narrow frequency ranges, this effect however can be neglected and we assume a constant $Q(f) = Q_0$. For the bulk of the Earth, the shear wave attenuation Q_μ^{-1} is significantly higher than the bulk attenuation Q_κ^{-1} , so a typical assumption is $Q_\kappa = \infty$. For a Poisson solid ($\alpha/\beta = \sqrt{3}$), this means $Q_P = 9/4 Q_\mu = 9/4 Q_S$. If the P- and the S-wave travel the same path, the ratio of their travel times is $\sqrt{3}$, resulting in $t_P^* \approx t_S^*/4$.

A full attenuation model of the Martian mantle and lithosphere including scattering does not exist yet, but we can assume that all LF marsquakes located in Cerberus Fossae are affected by the same attenuation structure. We therefore attempt to remove the effect of attenuation (eq. 4) by choosing a value for Q_μ that minimizes the difference between the P- and the S- spectrum for all LF marsquakes located in Cerberus Fossae. Following [17], we assume that the propagation path for HF events is shallow and different compared to the LF events and therefore, a different average Q_μ applies. After selecting these values for attenuation, we expect to be left with a reasonable estimate of the pure source spectrum, from which we can infer the corner frequency, f_c . Given the low signal-to-noise ratio and limited bandwidth of the Martian data (see fig. 4), we assume for simplicity that the corner frequencies for P- and S-waves are identical. Further, we fix $\gamma = 1$ and only try to match for f_c and n .

To summarize: We correct for attenuation using

$$A_S(f) = \underbrace{A_{0,S}}_{A_{\text{src},S}(f)} \underbrace{\frac{1}{1 + (f/f_c)^n} \exp\left(-\frac{\pi f T_S}{Q_S}\right)}_{A_{\text{att},S}(f)} \quad (5)$$

and

$$A_P(f) = \xi A_{\text{src},S}(f) A_{\text{att},S}^{-(1/4)}(f), \quad (6)$$

where ξ is the zero-frequency P/S ratio, which depends mainly on the focal mechanism, as well as on the wave velocities at the source. Since it is a constant offset, we fix it such, that the long-period part of P- and S-spectra match here.

We compute the spectra of P- and S-waves from a 30 second time window starting 10 seconds before the respective MQS pick. The short time window is chosen to mitigate the effect of lithospheric scattering. An additional noise spectrum is computed from a 60 second time window before the event to select a suitable frequency window for each individual event. The matching between observed $A_{\text{src},P}(f)$ and eq. 2 is done manually for each event. We find that a value of $Q_\mu = 1000$, equivalent to $Q_P = 2250$ produces a reasonable match between P- and S-wave spectra. This is not to be understood as a final value for the intrinsic attenuation of the mantle, but just as a value where source effects can be studied reasonably well. Figures 6 and 7 show that the value of $Q \approx 400$ proposed by [11] cannot explain both P- and S-spectra well and must be seen as an "effective Q", describing the spectral decay and thereby combining effects of source and structure (as written therein). The supplementary section A.5 contains figures of observed spectra and matching source functions for the events discussed in this manuscript. We manually match two corner frequencies f_c to each event, a reasonable maximum and minimum, with a fixed slope of $n = 2.5$. For the final dataset in table 1 and figure 4, we add an additional 0.1 to the uncertainty to account for the limited SNR of all events.

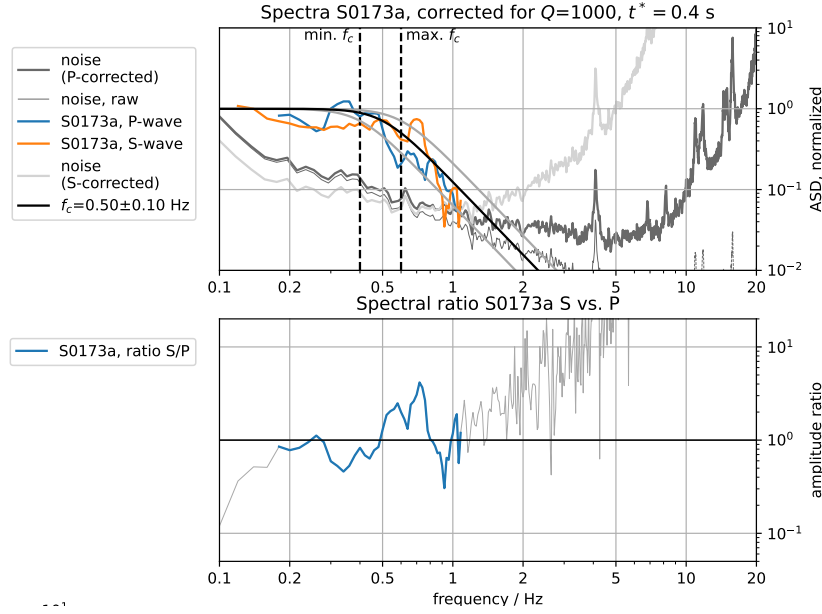


Figure 6: Event S0173a, after correction for Q_μ (eq. 5, 6). Top: The value of $Q_\mu = 1000$ has been chosen to make P and S-wave spectra match. Each spectrum was computed in a time window of 30 second length around the arrival using a multitaper method [77]. The S-wave and P-wave amplitude spectra meet the pre-event noise at 1.1 Hz. For easier comparison, the noise spectra are plotted 3 times: (i) raw, and using the correction terms for (ii) P- and (iii) S-waves. Bottom: Ratio of P- and S-wave spectrum. The colored part highlights the frequency range in which both P- and S-wave are above noise. The black line marks a theoretical spectrum (eq. 2) with $f_c = 0.5$ Hz and $n = 2$.

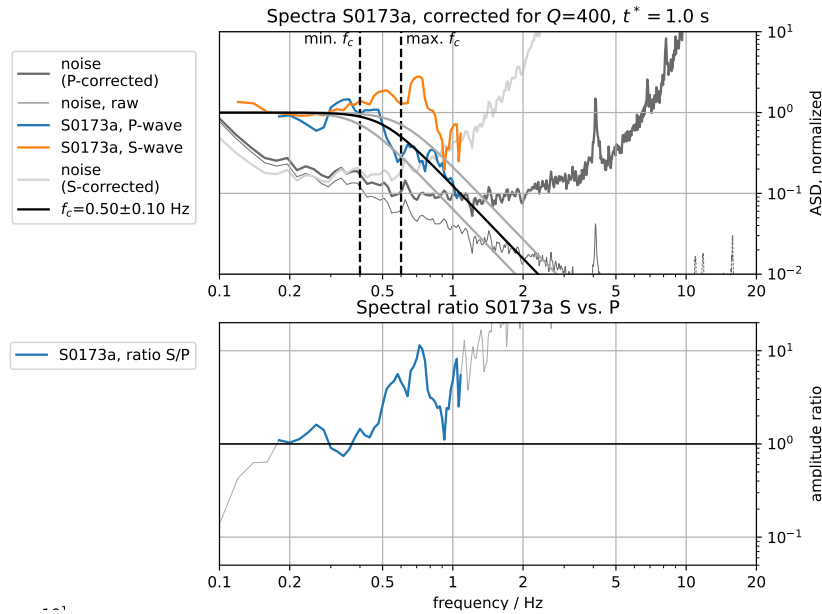


Figure 7: Event S0173a, with the attenuation model of [11]. The value of $Q_\mu = 400$ leads to a significant over-prediction of the S-wave amplitude above 0.5 Hz.

References:

1. Knapmeyer, M. *et al.* Working Models for Spatial Distribution and Level of Mars' Seismicity. *Journal of Geophysical Research E: Planets* **111**, 1–23 (2006).
2. Tanaka, K. L. *et al.* Geologic Map of Mars. *U.S. Geological Survey Geologic Investigations*, 3292–3292 (2014).
3. Lognonné, P. *et al.* SEIS: Insight's Seismic Experiment for Internal Structure of Mars. *Space Science Reviews* **215**, 12–12 (Jan. 2019).
4. Banerdt, W. B. *et al.* Initial Results from the InSight Mission on Mars. *Nature Geoscience* **13**, 183–189 (Mar. 2020).
5. Golombek, M. P. *et al.* Geology of the InSight Landing Site on Mars. *Nature Communications* **11**, 1–11 (2020).
6. Phillips, R. J. *Expected Rate of Marsquakes* tech. rep. (1991), 35–38.
7. Gudkova, T. V., Batov, A. V. & Zharkov, V. N. Model Estimates of Non-Hydrostatic Stresses in the Martian Crust and Mantle: 1—Two-Level Model. *Solar System Research* **51**, 457–478 (Nov. 2017).
8. Berman, D. C. & Hartmann, W. K. Recent Fluvial, Volcanic, and Tectonic Activity on the Cerberus Plains of Mars. *Icarus* **159**, 1–17 (Sept. 2002).
9. Anderson, R. C. *et al.* Primary Centers and Secondary Concentrations of Tectonic Activity through Time in the Western Hemisphere of Mars. *Journal of Geophysical Research: Planets* **106**, 20563–20585 (2001).
10. Lognonné, P. *et al.* Constraints on the Shallow Elastic and Anelastic Structure of Mars from InSight Seismic Data. *Nature Geoscience* **13**, 213–220 (Mar. 2020).
11. Giardini, D. *et al.* The Seismicity of Mars. *Nat. Geosci.* **13**, 205–212 (Mar. 2020).
12. Brinkman, N. *et al.* First Focal Mechanisms of Marsquakes. *Journal of Geophysical Research: Planets* (2021).
13. Clinton, J. F. *et al.* The Marsquake Catalogue from InSight, Sols 0–478. *Physics of the Earth and Planetary Interiors* **310** (2021).
14. Service, I. M. *Mars Seismic Catalogue, InSight Mission; V6 2021-04-01* 2021.
15. Jacob, A. *et al.* Seismic Sources of InSight Marsquakes and Seismotectonic Context of Elysium Planitia, Mars. *Tectonophysics*, 229434 (June 2022).
16. Stähler, S. C. *et al.* Seismic Detection of the Martian Core. *Science* **373**, 443–448 (July 2021).
17. van Driel, M. *et al.* High-Frequency Seismic Events on Mars Observed by InSight. *Journal of Geophysical Research: Planets* **126**, e2020JE006670 (2021).
18. Horleston, A. *et al.* The Far Side of Mars - Two Distant Marsquakes Detected by InSight. *The seismic record* **2**, 88–99 (2022).
19. Perrin, C. *et al.* Geometry and Segmentation of Cerberus Fossae, Mars: Implications for Marsquake Properties. *Journal of Geophysical Research: Planets* **127**, e2021JE007118 (2022).
20. Head, J. W. Generation of Recent Massive Water Floods at Cerberus Fossae, Mars by Dike Emplacement, Cryospheric Cracking, and Confined Aquifer Groundwater Release. *Geophys. Res. Lett.* **30**, 1577 (2003).
21. Burr, D. M. Recent Aqueous Floods from the Cerberus Fossae, Mars. *Geophys. Res. Lett.* **29**, 1013 (2002).
22. Taylor, J., Teanby, N. A. & Wookey, J. Estimates of Seismic Activity in the Cerberus Fossae Region of Mars. *Journal of Geophysical Research E: Planets* **118**, 2570–2581 (2013).
23. Voigt, J. R. C. & Hamilton, C. W. Investigating the Volcanic versus Aqueous Origin of the Surficial Deposits in Eastern Elysium Planitia, Mars. *Icarus* **309**, 389–410 (July 2018).
24. Horvath, D. G., Moitra, P., Hamilton, C. W., Craddock, R. A. & Andrews-Hanna, J. C. Evidence for Geologically Recent Explosive Volcanism in Elysium Planitia, Mars. *Icarus* **365**, 114499 (Sept. 2021).
25. Banerdt, W. B., Golombek, M. P. & Tanaka, K. L. Stress and Tectonics on Mars. In: *Mars (A93-27852 09-91)*, p. 249–297., 249–297 (1992).
26. Hauber, E., Brož, P., Jagert, F., Jodłowski, P. & Platz, T. Very Recent and Wide-Spread Basaltic Volcanism on Mars. *Geophysical Research Letters* **38**, n/a–n/a (2011).
27. Plesa, A.-C., Wiczeorek, M., Knapmeyer, M., Walterova, M. & Breuer, D. in *Geophysical Exploration of the Solar System* (Elsevier, May 2022).
28. Zenhäusern, G. *et al.* Low-Frequency Marsquakes and Where to Find Them: Back Azimuth Determination Using a Polarization Analysis Approach. *Bulletin of the Seismological Society of America* (May 2022).
29. Stähler, S. C., Khan, A., Drilleau, M., Duran, A. C. & Samuel, H. *Interior Models of Mars from Inversion of Seismic Body Waves* 2021.
30. Böse, M. *et al.* Magnitude Scales for Marsquakes Calibrated from InSight Data. *Bulletin of the Seismological Society of America* (June 2021).

31. Knapmeyer, M. *et al.* Seasonal Seismic Activity on Mars. *Earth and Planetary Science Letters* **576**, 117171 (Dec. 2021).
32. Knapmeyer, M. *et al.* Estimation of the Seismic Moment Rate from an Incomplete Seismicity Catalog, in the Context of the InSight Mission to Mars. *Bulletin of the Seismological Society of America* **109**, 1125–1147 (2019).
33. Knapmeyer-Endrun, B. *et al.* Thickness and Structure of the Martian Crust from InSight Seismic Data. *Science* **373**, 438–443 (July 2021).
34. Vetterlein, J. & Roberts, G. P. Structural Evolution of the Northern Cerberus Fossae Graben System, Elysium Planitia, Mars. *Journal of Structural Geology* **32**, 394–406 (Apr. 2010).
35. Brune, J. N. Tectonic Stress and the Spectra of Seismic Shear Waves from Earthquakes. *Journal of Geophysical Research (1896-1977)* **75**, 4997–5009 (1970).
36. Abercrombie, R. E. Earthquake Source Scaling Relationships from -1 to 5 ML Using Seismograms Recorded at 2.5-Km Depth. *Journal of Geophysical Research: Solid Earth* **100**, 24015–24036 (1995).
37. Allmann, B. P. & Shearer, P. M. Global Variations of Stress Drop for Moderate to Large Earthquakes. *Journal of Geophysical Research: Solid Earth* **114** (2009).
38. Compaire, N. *et al.* Autocorrelation of the Ground Vibrations Recorded by the SEIS-InSight Seismometer on Mars. *Journal of Geophysical Research: Planets* **126**, e2020JE006498 (2021).
39. Laske, G., Masters, G., Ma, Z. & Pasyanos, M. *Update on CRUST1.0 - A 1-Degree Global Model of Earth's Crust in Geophysical Research Abstracts* (2013), EGU2013–2658.
40. Durán, C. *et al.* Seismology on Mars: An Analysis of Direct, Reflected, and Converted Seismic Body Waves with Implications for Interior Structure. *Physics of the Earth and Planetary Interiors* **325**, 106851 (Apr. 2022).
41. Drilleau, M. *et al.* Marsquake Locations and 1-D Seismic Models for Mars from InSight Data. *Journal of Geophysical Research (Planets)* **accepted** (2022).
42. Abercrombie, R. E. Resolution and Uncertainties in Estimates of Earthquake Stress Drop and Energy Release. *Philosophical Transactions of the Royal Society A: Mathematical, Physical and Engineering Sciences* **379**, 20200131 (May 2021).
43. Giampiccolo, E., D'Amico, S., Patane, D. & Gresta, S. Attenuation and Source Parameters of Shallow Microearthquakes at Mt. Etna Volcano, Italy. *Bulletin of the Seismological Society of America* **97**, 184–197 (Feb. 2007).
44. Vallée, M. Source Time Function Properties Indicate a Strain Drop Independent of Earthquake Depth and Magnitude. *Nature Communications* **4**, 2606–2606 (2013).
45. Oberst, J. Unusually High Stress Drops Associated with Shallow Moonquakes. *Journal of Geophysical Research* **92**, 1397–1405 (1987).
46. Hensch, M. *et al.* Deep Low-Frequency Earthquakes Reveal Ongoing Magmatic Recharge beneath Laacher See Volcano (Eifel, Germany). *Geophysical Journal International* **216**, 2025–2036 (Mar. 2019).
47. Chouet, B. A. & Matoza, R. S. A Multi-Decadal View of Seismic Methods for Detecting Precursors of Magma Movement and Eruption. *Journal of Volcanology and Geothermal Research* **252**, 108–175 (Feb. 2013).
48. Kedar, S. *et al.* Analyzing Low Frequency Seismic Events at Cerberus Fossae as Long Period Volcanic Quakes. *Journal of Geophysical Research: Planets* **126**, e2020JE006518 (2021).
49. Madariaga, R. Dynamics of an Expanding Circular Fault. *Bulletin of the Seismological Society of America* **66**, 639–666 (1976).
50. Roberts, G. P., Matthews, B., Bristow, C., Guerrieri, L. & Vetterlein, J. Possible Evidence of Paleomarsquakes from Fallen Boulder Populations, Cerberus Fossae, Mars. *Journal of Geophysical Research: Planets* **117**, n/a–n/a (Feb. 2012).
51. Kolzenburg, S. *et al.* Solid as a Rock: Tectonic Control of Graben Extension and Dike Propagation. *Geology* **50**, 260–265 (Nov. 2021).
52. Watters, T. R. *et al.* Shallow Seismic Activity and Young Thrust Faults on the Moon. *Nature Geoscience* **12**, 411–417 (2019).
53. Plesa, A.-C. *et al.* Present-Day Mars' Seismicity Predicted From 3-D Thermal Evolution Models of Interior Dynamics. *Geophysical Research Letters* **45**, 2580–2589 (Mar. 2018).
54. Bergman, E. A. Intraplate Earthquakes and the State of Stress in Oceanic Lithosphere. *Tectonophysics* **132**, 1–35 (Dec. 1986).
55. Clauser, C. & Huenges, E. in *Rock Physics & Phase Relations* 105–126 (American Geophysical Union (AGU), 1995). ISBN: 978-1-118-66810-8.
56. Khan, A. *et al.* Imaging the Upper Mantle Structure of Mars with InSight Seismic Data. *Science* **373**, 434–438 (2021).

57. Byrne, P. K. A Comparison of Inner Solar System Volcanism. *Nature Astronomy* **4**, 321–327 (2020).
58. Smith, D. E. *et al.* Mars Orbiter Laser Altimeter: Experiment Summary after the First Year of Global Mapping of Mars. *Journal of Geophysical Research: Planets* **106**, 23689–23722 (2001).
59. Dahmen, N. L. *et al.* Resonances and Lander Modes Observed by InSight on Mars (1–9 Hz). *Bulletin of the Seismological Society of America* **111**, 2924–2950 (Oct. 2021).
60. Hobiger, M. *et al.* The Shallow Structure of Mars at the InSight Landing Site from Inversion of Ambient Vibrations. *Nat Commun* **12**, 6756 (Nov. 2021).
61. Iio, Y. SCALING RELATION BETWEEN EARTHQUAKE SIZE AND DURATION OF FAULTING FOR SHALLOW EARTHQUAKES IN SEISMIC MOMENT BETWEEN 10^{10} AND 10^{25} Dyne•cm. *Journal of Physics of the Earth* **34**, 127–169 (1986).
62. Bilek, S. L., Lay, T. & Ruff, L. J. Radiated Seismic Energy and Earthquake Source Duration Variations from Teleseismic Source Time Functions for Shallow Subduction Zone Thrust Earthquakes. *Journal of Geophysical Research: Solid Earth* **109** (2004).
63. Matsuzawa, T., Obara, K. & Maeda, T. Source Duration of Deep Very Low Frequency Earthquakes in Western Shikoku, Japan. *Journal of Geophysical Research: Solid Earth* **114** (2009).
64. Clinton, J. F. *et al.* The Marsquake Service: Securing Daily Analysis of SEIS Data and Building the Martian Seismicity Catalogue for InSight. *Space Science Reviews* **214**, 133–133 (Dec. 2018).
65. Böse, M. *et al.* A Probabilistic Framework for Single-Station Location of Seismicity on Earth and Mars. *Physics of the Earth and Planetary Interiors* **262**, 48–65 (2016).
66. Schimmel, M. & Gallart, J. The Use of Instantaneous Polarization Attributes for Seismic Signal Detection and Image Enhancement. *Geophysical Journal International* **155**, 653–668 (2003).
67. Kim, D. *et al.* Improving Constraints on Planetary Interiors With PPs Receiver Functions. *Journal of Geophysical Research: Planets* **126**, e2021JE006983 (2021).
68. VanDecar, J. C. & Crosson, R. S. Determination of Teleseismic Relative Phase Arrival Times Using Multi-Channel Cross-Correlation and Least Squares. *Bulletin of the Seismological Society of America* **80**, 150–169 (Feb. 1990).
69. Kane, D. L., Prieto, G., Vernon, F. L. & Shearer, P. M. Quantifying Seismic Source Parameter Uncertainties. *Bulletin of the Seismological Society of America* **101**, 535–543 (Mar. 2011).
70. Trugman, D. T., Dougherty, S. L., Cochran, E. S. & Shearer, P. M. Source Spectral Properties of Small to Moderate Earthquakes in Southern Kansas. *Journal of Geophysical Research: Solid Earth* **122**, 8021–8034 (2017).
71. Aki, K. & Chouet, B. Origin of Coda Waves: Source, Attenuation, and Scattering Effects. *Journal of Geophysical Research* **80**, 3322–3342 (1975).
72. Yoshimoto, K., Sato, H. & Ohtake, M. Frequency-Dependent Attenuation of P and S Waves in the Kanto Area, Japan, Based on the Coda-Normalization Method. *Geophysical Journal International* **114**, 165–174 (July 1993).
73. Nakamura, Y. & Koyama, J. Seismic Q of the Lunar Upper Mantle. *Journal of Geophysical Research* **87**, 4855–4861 (1982).
74. Boatwright, J. Seismic Estimates of Stress Release. *Journal of Geophysical Research: Solid Earth* **89**, 6961–6968 (Aug. 1984).
75. Kaneko, Y. & Shearer, P. M. Seismic Source Spectra and Estimated Stress Drop Derived from Cohesive-Zone Models of Circular Subshear Rupture. *Geophysical Journal International* **197**, 1002–1015 (May 2014).
76. Baig, A. M., Dahlen, F. A. & Hung, S.-H. Traveltimes of Waves in Three-Dimensional Random Media. *Geophysical Journal International* **153**, 467–482 (May 2003).
77. Prieto, G., Parker, R. L. & Vernon, F. L. A Fortran 90 Library for Multitaper Spectrum Analysis. *Computers & Geosciences* **35**, 1701–1710 (Aug. 2009).
78. Ceylan, S. *et al.* Companion Guide to the Marsquake Catalog from InSight, Sols 0–478: Data Content and Non-Seismic Events. *Physics of the Earth and Planetary Interiors* **310**, 106597–106597 (Jan. 2021).
79. Scholz, J.-R. *et al.* Detection, Analysis, and Removal of Glitches From InSight’s Seismic Data From Mars. *Earth and Space Science* **7**, 1–31 (Nov. 2020).
80. Kim, D. *et al.* Potential Pitfalls in the Analysis and Structural Interpretation of Seismic Data from the Mars InSight Mission. *Bulletin of the Seismological Society of America* **111**, 2982–3002 (Oct. 2021).
81. Kagan, Y. Y. Seismic Moment Distribution Revisited: I. Statistical Results. *Geophysical Journal International* **148**, 520–541 (Mar. 2002).

A Supplement

A.1 Distribution of marsquakes

Probability density functions for distance and back azimuth for LF events are taken from models in [29] and [28]. Figure 2 only shows distance distributions for all investigated events using different interior models, thus leading to far and near end-member models and a mean model. In Figure 1 we multiply the normalized mean distance and back-azimuth distributions. For HF, we show the distance distribution in Figure 2a. For Figure 1, we use a back azimuth of 78 ± 12 deg (see A.2) and the black box highlights the 80% density line inferred for by distance estimates within the back-azimuth range.

A.2 Back azimuth estimates of the HF event cluster

All Marsquake Service (MQS) HF events with event quality C or above are used in this analysis [14]. For each event, we use a standard algorithm of STA/LTA (Short Time Average over Long Time Average) triggering on the corresponding energy envelope averaged across ZNE components to pick Pg- and Sg-arrivals [hereby referred as the MQS picks, e.g. 11, 13]. Here, our energy envelope is computed for instrument-removed velocity waveforms in the spectral domain using a 30 s window with 90% overlap. We remove noticeable glitches and donks [see detailed description of these electro-mechanical signals in e.g. 78–80] within our analysis window between the Pg- and Sg-arrival times. In addition, we discard those events for which spectral envelopes significantly deviate from the mean envelope of all HF event data. 62 out of 116 events with corresponding correlation coefficients < 0.8 are therefore not considered in the analysis. Next, the initial alignment guided by the MQS picks is refined for both Pg- and Sg-arrival times systematically using an implementation of a multichannel cross-correlation method [68] in order to obtain precisely aligned waveform data with our updated picks (Fig. 8A-B). A pick uncertainty is assigned based on the duration of the amplitude rise time for each spectral envelope (starting from the onset until the amplitude reaches its maximum). Figure 8C shows the comparison of the relocated vs. the MQS distance estimates with velocities of $v_{Pg} = 4$ km/s and $v_{Pg}/v_{Sg} = \sqrt{3}$. The observed difference in the two sets of distance estimates is small, with the mean and standard deviation of the MQS vs. relocated distances being 24.7 ± 2.9 deg and 24.0 ± 2.6 deg, respectively. To estimate the dominant direction of seismic energy traveling from the HF event cluster, we perform a grid search on back azimuths that maximize the median power ratio between the radial vs. transverse component within -30 s to 30 s of the aligned Pg-arrivals across multiple HF events simultaneously (e.g., data bounded by the red lines in Fig. 8A-B). A similar approach has been successfully applied to individual LF/BB marsquake data in a recent receiver function analysis [10, 33, 67]. Further, we apply a 2 s moving-window to compute the power ratio at each time for all 62 HF events and obtain the weighted median power ratio. In this process, we use relative weights for our HF events based on the signal-to-noise of each individual event. The average background power ratio is estimated by (i) stacking those values computed within the pre-event noise window (i.e., values between -30 s and 0 s) and (ii) subtracting those from our resulting power ratios (Fig. 9). Our back azimuth search on HF data aligned by the MQS picks did not show any prominent arrivals in the -30 to 30 s search window (Fig. 9A). However, we observe that the maximum power ratio is strongly focused at the back azimuth value of 78 ± 12 deg once our events are systematically re-aligned (c.f., Fig. 9A-B) despite a number of weak scattered maxima in the time window. Notably, energy arriving after ≈ 20 s becomes much more apparent when we repeat the analysis using a subgroup of HF events which forms the largest sample size within the event cluster (Fig. 9C). The time axis in this plot is shifted arbitrarily due to the realignment.

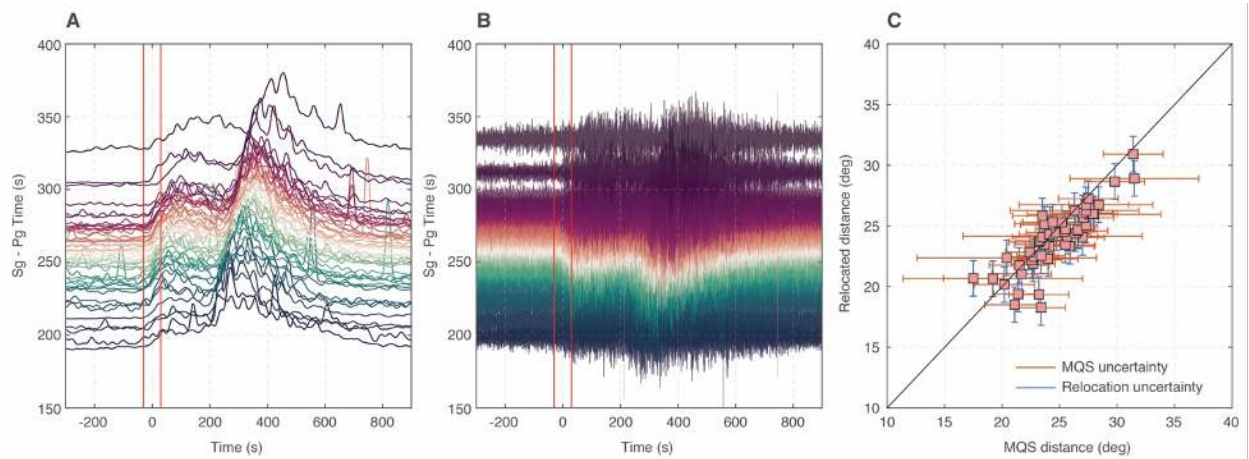


Figure 8: (A) Average three-component envelopes aligned on Pg-arrival ($t = 0$ s) from a total of 62 marsquakes from the HF event category, and the corresponding (B) vertical component waveforms. All MQS events with the event quality C or above are selected between Sols 128 and 1050 [14] but those with low envelope similarity (i.e., correlation coefficient < 0.8 against the mean envelope of all HF event data) are removed. (C) Comparison of the MQS vs. relocated distance estimates with $v_{Pg}=4$ km/s and $v_{Pg}/v_{Sg}=\sqrt{3}$.

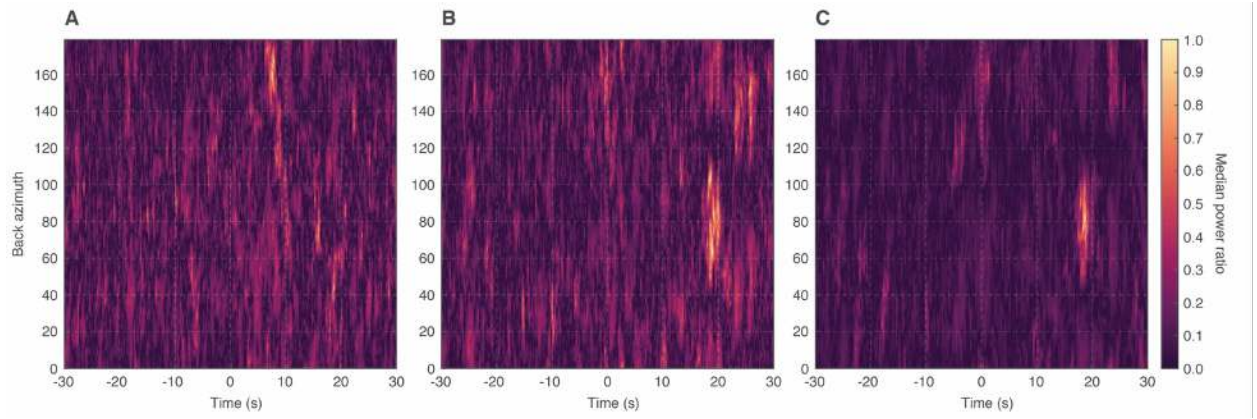


Figure 9: Median power ratio between radial and transverse components of the HF waveforms (A) before, and (B) after applying the re-alignment using average spectral envelopes. (C) Same as (B) but using a subgroup of HF events that clustered tightly at the mean relocated distance of 24° . Background power which is strongly affected by wind noise and lander resonances is removed.

A.3 Estimating total moment rate

Estimating the long term average moment release rate from an incomplete catalog is affected by the annual variability of moment release that even a perfectly Poissonian distribution of quakes shows.

We first test the distribution for derivation from a Poisson process, by plotting the cumulative count of events over time and the lag time between events (Fig. 10) and while we find an increased rate in the second year, both years show no significant deviation from a Poisson process. For the annual rate, we follow the approach presented in [32] to estimate the parameters of a tapered Gutenberg-Richter size-frequency distribution [81]: The cumulative number of earthquakes Φ above a magnitude M is then given by

$$\Phi(M) = \left(\frac{M_t}{M}\right)^\beta \exp\left(\frac{M_t - M}{M_c}\right) \quad (7)$$

In this equation, β is the slope of the power law, describing the distribution of larger to smaller quakes, M_t describes the magnitude above which the distribution tapers, i.e. larger events occur less often than expected by the power law and M_c is the magnitude of completeness of the catalog. The total annual moment release \dot{M}_S can then be estimated from these parameters, as described in [32].

For the events observed in Cerberus Fossae, we assume a slope $\beta = 2/3$, equivalent to a b -value of 1. We use the KS_{10} estimator from [32] that uses the 10 largest events of a catalog with unknown M_c . We further need to take into account that only during 26% of the observation time, the local atmospheric conditions were quiet enough to observe marsquakes. To account for magnitude uncertainty, the analysis was repeated 10,000 times with individual event magnitudes randomly varied according to their estimated uncertainty [30] in the MQS catalog v9.

The resulting estimate of corner magnitude and moment rate are shown in Figure 11, using the KS_{10} estimator of [32], in the same style as Figures 4, 7 therein. The estimated long term moment rate is $2.93 \cdot 10^{15}$ Nm/a, with an 80% interval between $1.35 \cdot 10^{15}$ Nm/a and $5.52 \cdot 10^{15}$ Nm/a (Figure 12).

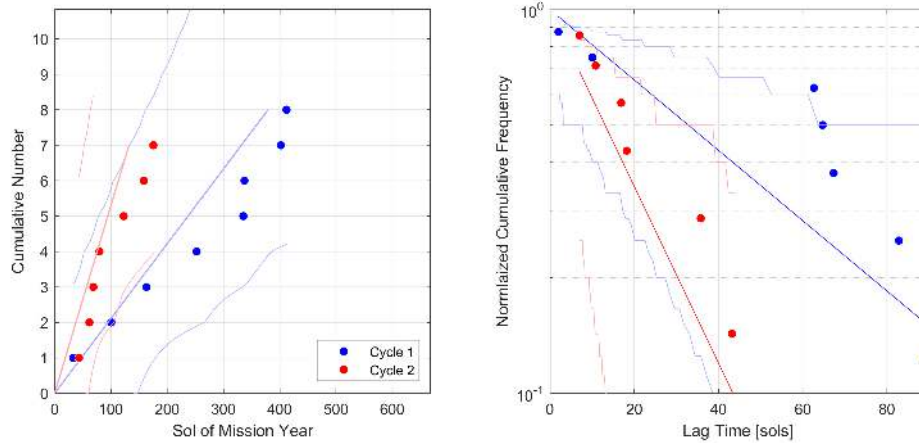


Figure 10: Cumulative count of events (left), and lag time distribution (right). For a stationary Poisson process, the cumulative count as function of time should follow a straight line in linear coordinates. The event rate defines the slope of this line. For the first year of operation (cycle 1, blue), we corrected the count after the three weeks down time in August/September 2019 by assuming that the rate during the down time equalled that afterwards. After Sol 400, increasing wind speeds at night made detection impossible until the second Martian year, starting around Sol 700. For the second year (cycle 2), no such correction was necessary. Pale lines indicate the nominal slope (cycle 1: 0.021 ± 0.007 events/sol, cycle 2: 0.053 ± 0.02 events/sol) and the 95% confidence intervals for likely scatter. The event series end with the end of the catalog (MQS v9). The lag times of a stationary Poisson process are exponentially distributed and thus follow a straight line in a semi-logarithmic plot. Lag times shorter than 1 sol were not considered; the daily noise regime makes them unreliable. All confidence were intervals estimated numerically from $1e5$ synthetic event sequences with the same rate and covering the same duration.

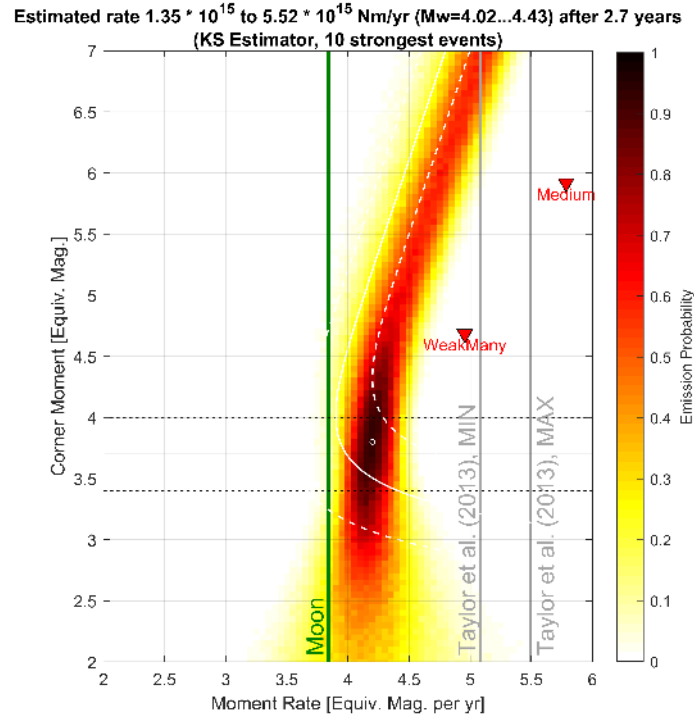


Figure 11: Emission probability of moment rate and corner moment taking into account the 10 largest events observed over the mission until 2021-12-31, using the KS10 estimator of [32], in the same style as figs. 4, 7 therein. For orientation, the moment release of the whole moon, as seen by the Apollo seismic network over 7 years of operation [45] (green) and the moment rates estimated by [22] for Cerberus Fossae (grey) are shown, as well as 2 global estimates from [1] (Many weak faults and the medium model).

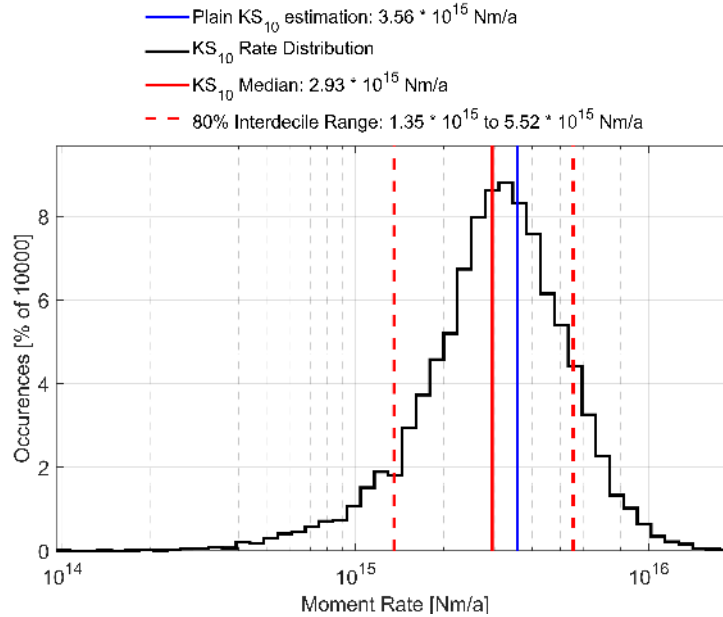


Figure 12: Distribution of annual moment release rate \dot{M} resulting from the emission probability in Figure 11.

543 **A.4 Global fault map**

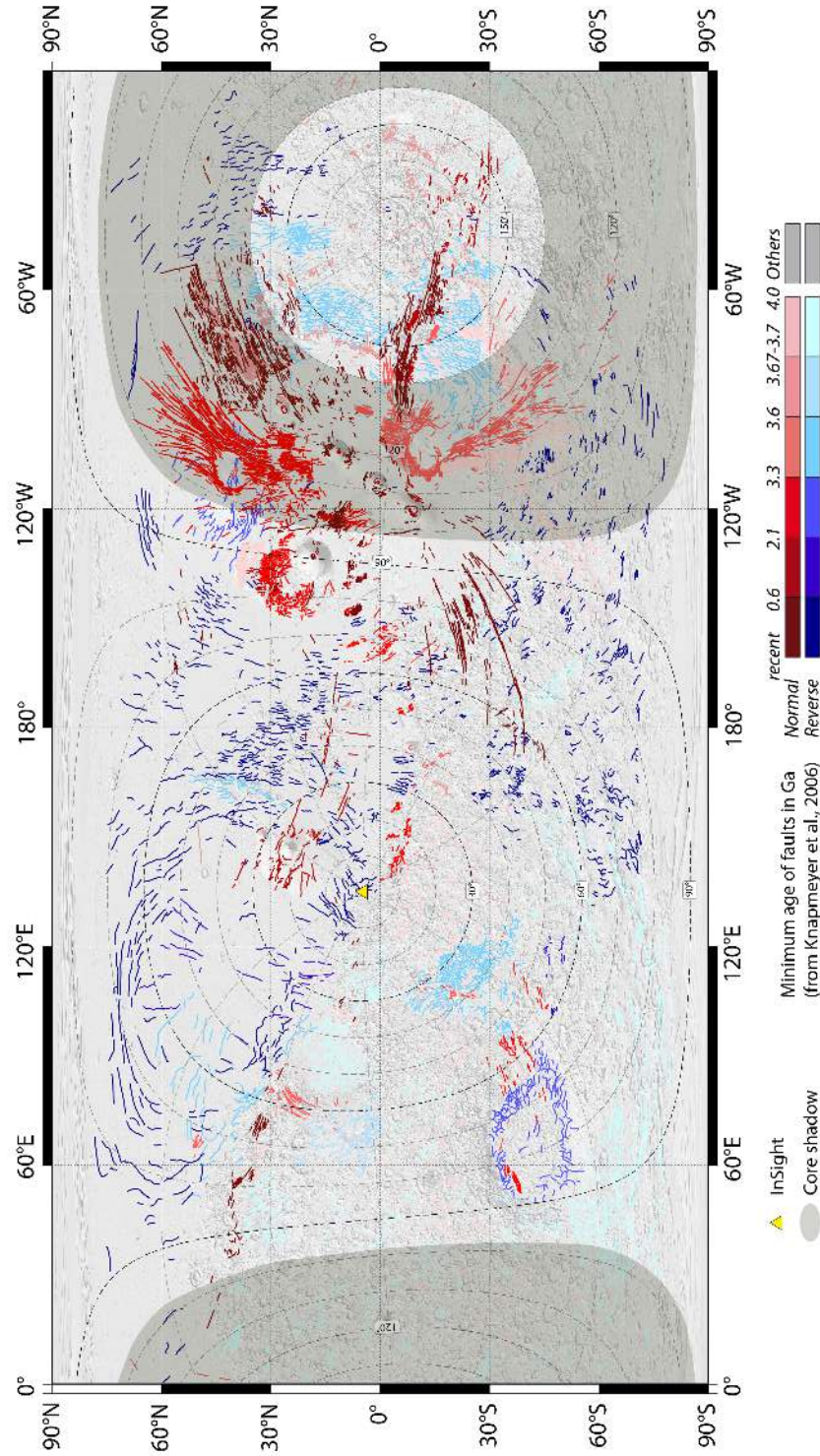


Figure 13: Global map of faults color-coded by minimum age [1, 2, 58]. The darkened area marks the core shadow [16], in which no direct body waves can be observed as seen from InSight. Thus event detection is significantly more difficult.

544 **A.5 Figures of spectral matching**

545 **A.5.1 Events in Cerberus Fossae**

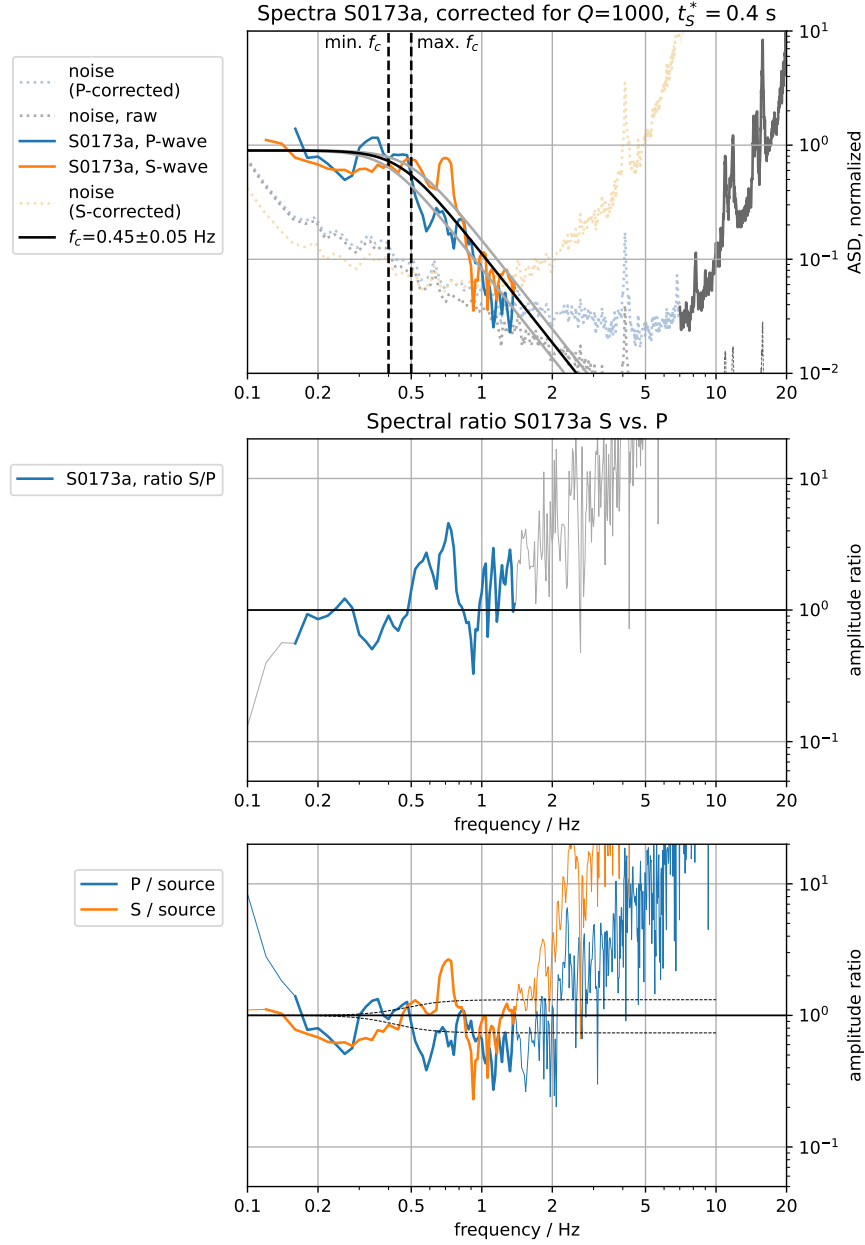


Figure 14: Event S0173a, after correction for Q_μ (eq. 5, 6). Top: The value of $Q_\mu = 1000$ has been chosen to make P and S-wave spectra match after attenuation correction. Each spectrum was computed in a time window of 30 second length around the arrival (-10s to 20s) using a multitaper method [77]. The S-wave and P-wave amplitude spectra meet the pre-event noise at 1.1 Hz. For easier comparison, P and S spectra are normalized individually and the noise spectra are plotted 3 times: (i) raw, and using the correction terms for (ii) P- and (iii) S-waves. The black line marks a theoretical spectrum (eq. 2) with $f_c = 0.45$ Hz and $n = 2.5$. Grey lines mark the range of source spectra visually compatible with the data, as an estimation of the uncertainty. Middle: Ratio of P- and S-wave spectrum. The colored part highlights the frequency range in which both P- and S-wave are above noise. Bottom: P- and S-wave spectra after correcting for source and attenuation. The dashed lines mark the expected values given the uncertainty in f_c . The curve is supposed to be flat until the pre-event noise level is reached (see top subplot).

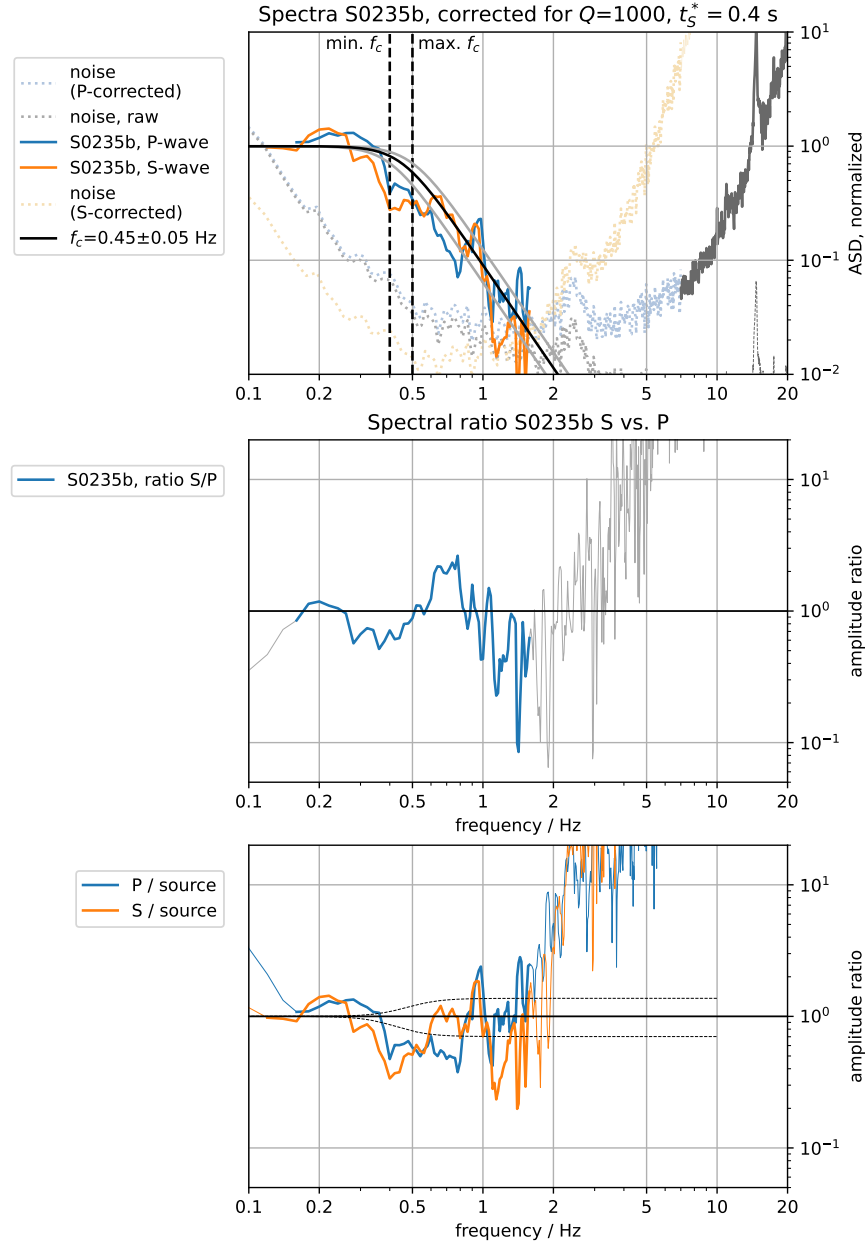


Figure 15: Event S0235b, after correction for Q_μ (eq. 5, 6). Plot is otherwise identical to 14

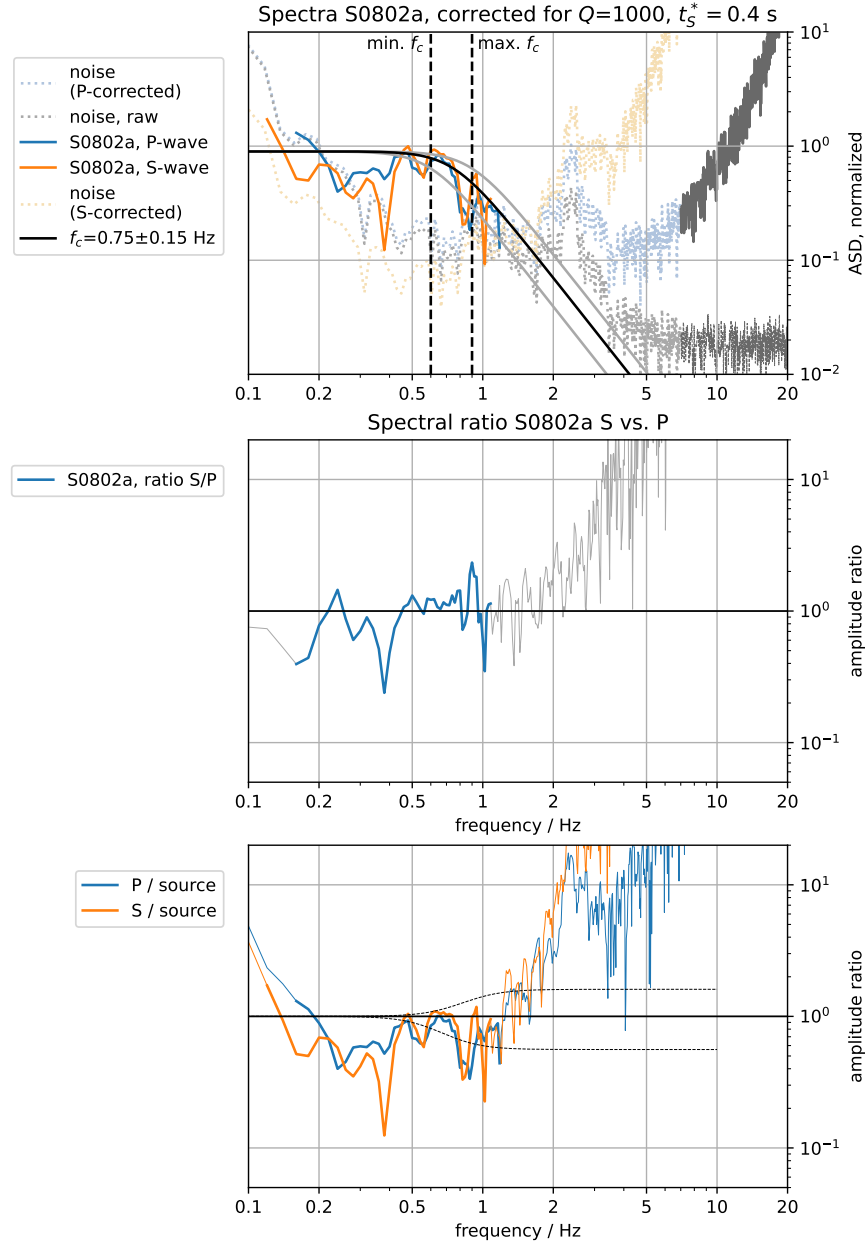


Figure 16: Event S0802a, after correction for Q_μ (eq. 5, 6). Plot is otherwise identical to 14

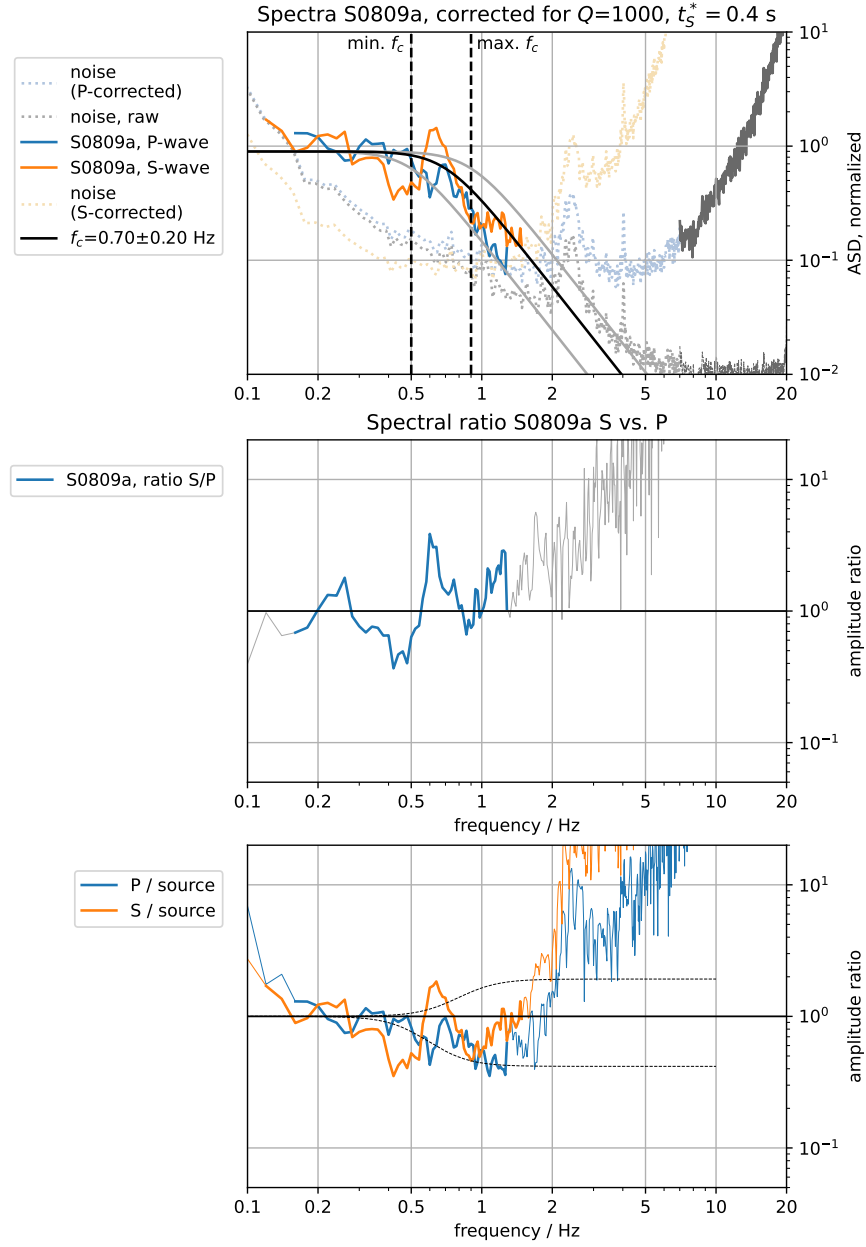


Figure 17: Event S0809a after correction for Q_μ (eq. 5, 6). Plot is otherwise identical to 14

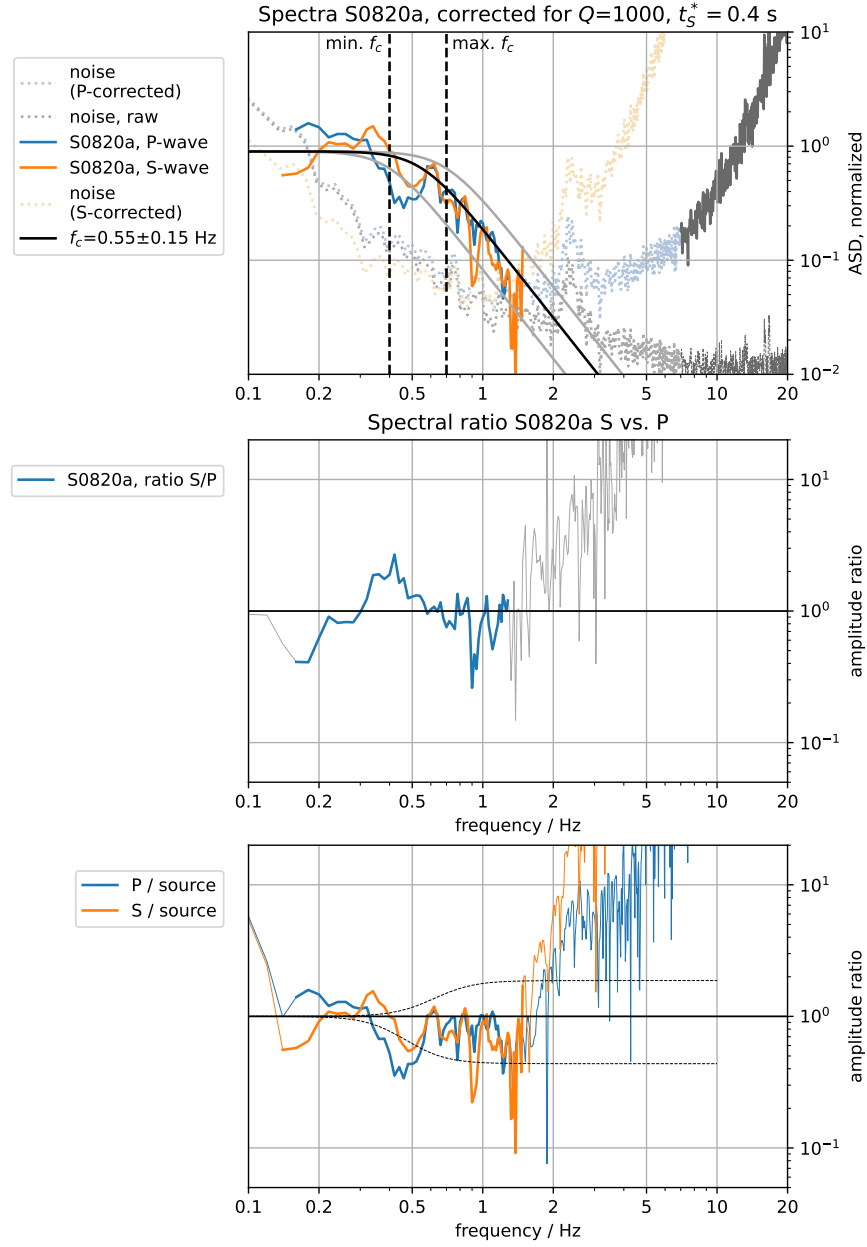


Figure 18: Event S0820a, after correction for Q_μ (eq. 5, 6). Plot is otherwise identical to 14

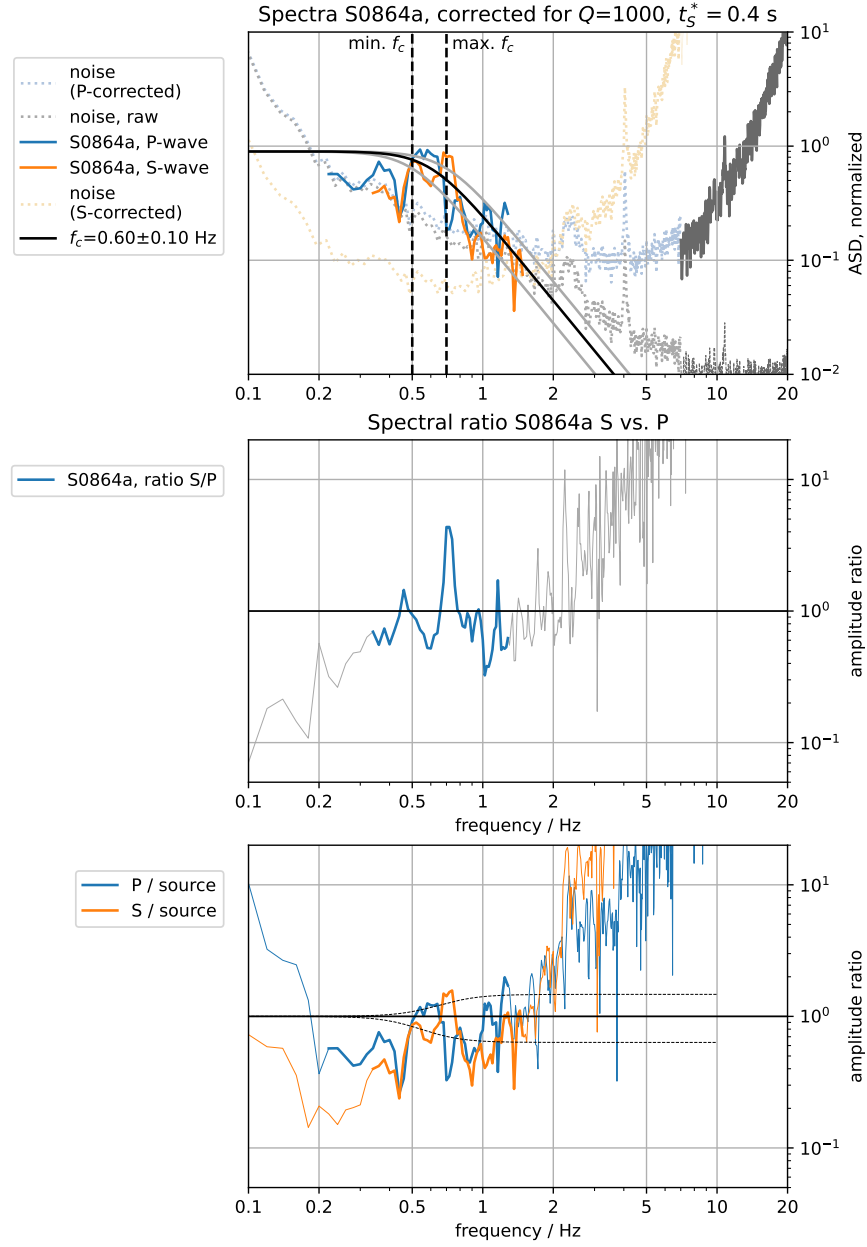


Figure 19: Event S0864a, after correction for Q_μ (eq. 5, 6). Plot is otherwise identical to 14

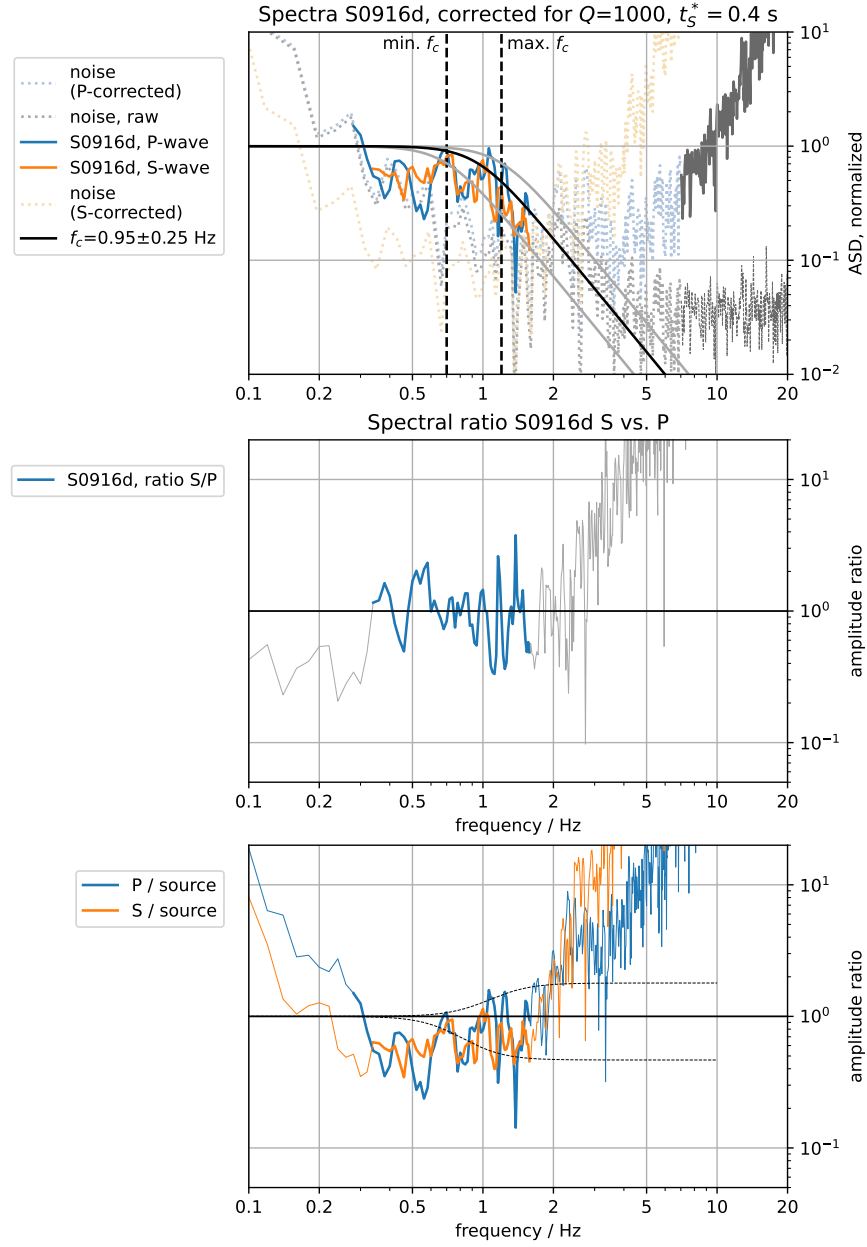


Figure 20: Event S0916d, after correction for Q_μ (eq. 5, 6). Plot is otherwise identical to 14

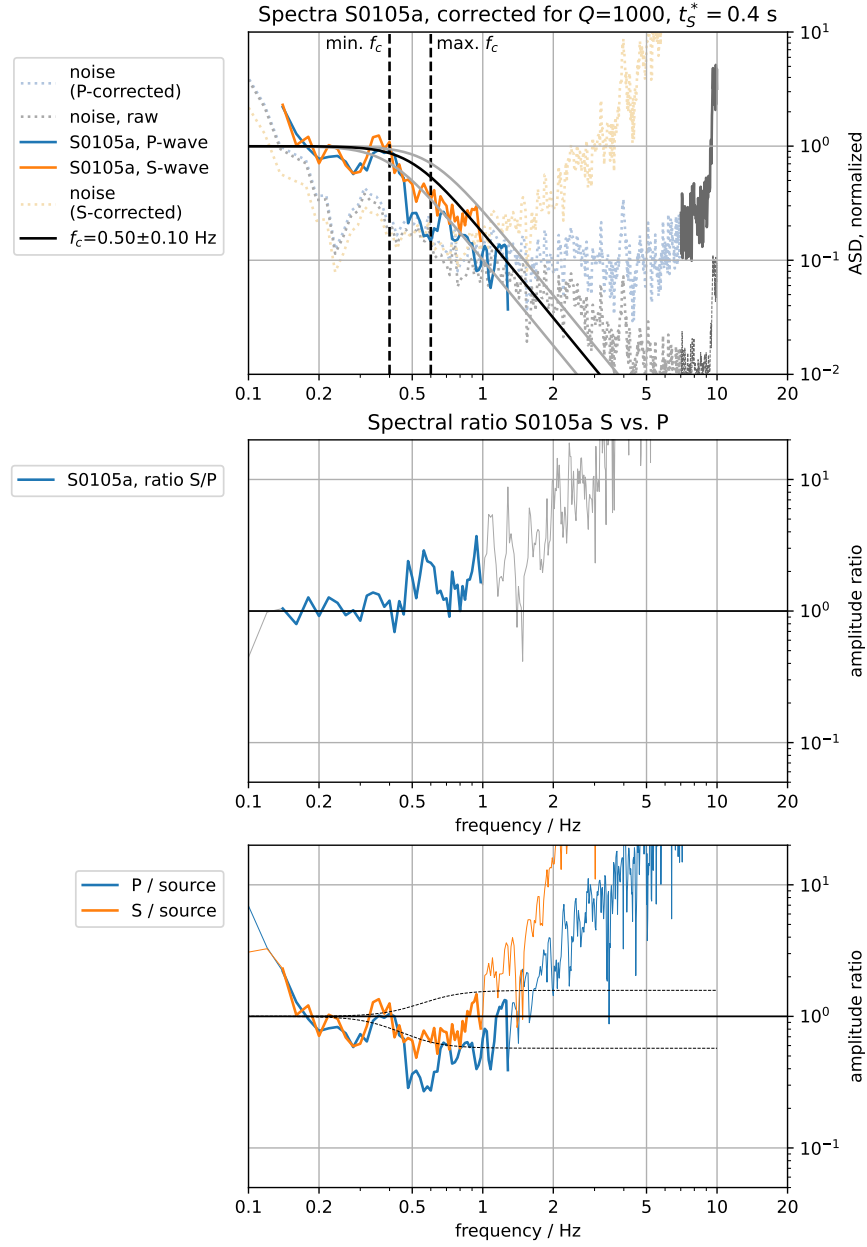


Figure 21: Event S0105a, after correction for Q_μ (eq. 5, 6). Plot is otherwise identical to 14

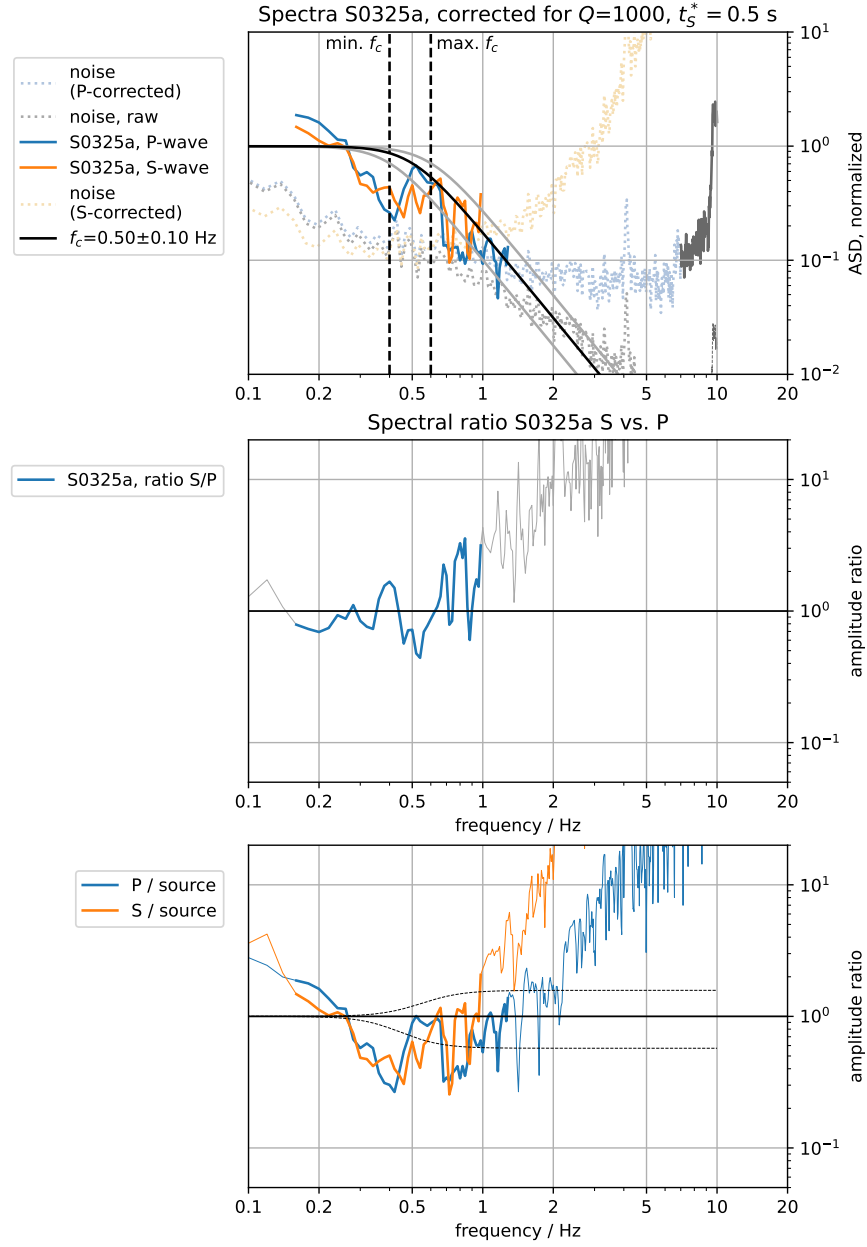


Figure 22: Event S0325a, after correction for Q_μ (eq. 5, 6). Plot is otherwise identical to 14

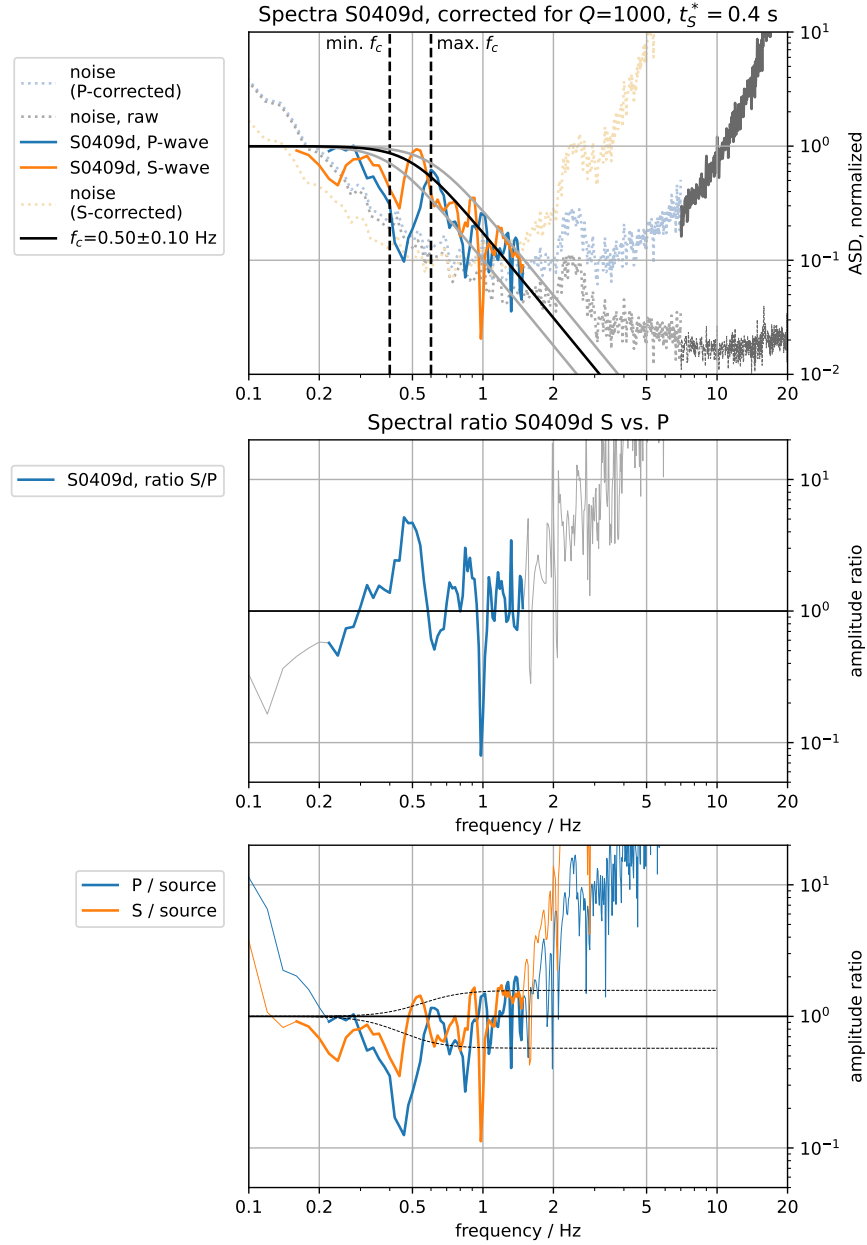


Figure 23: Event S0409d, after correction for Q_μ (eq. 5, 6). Plot is otherwise identical to 14

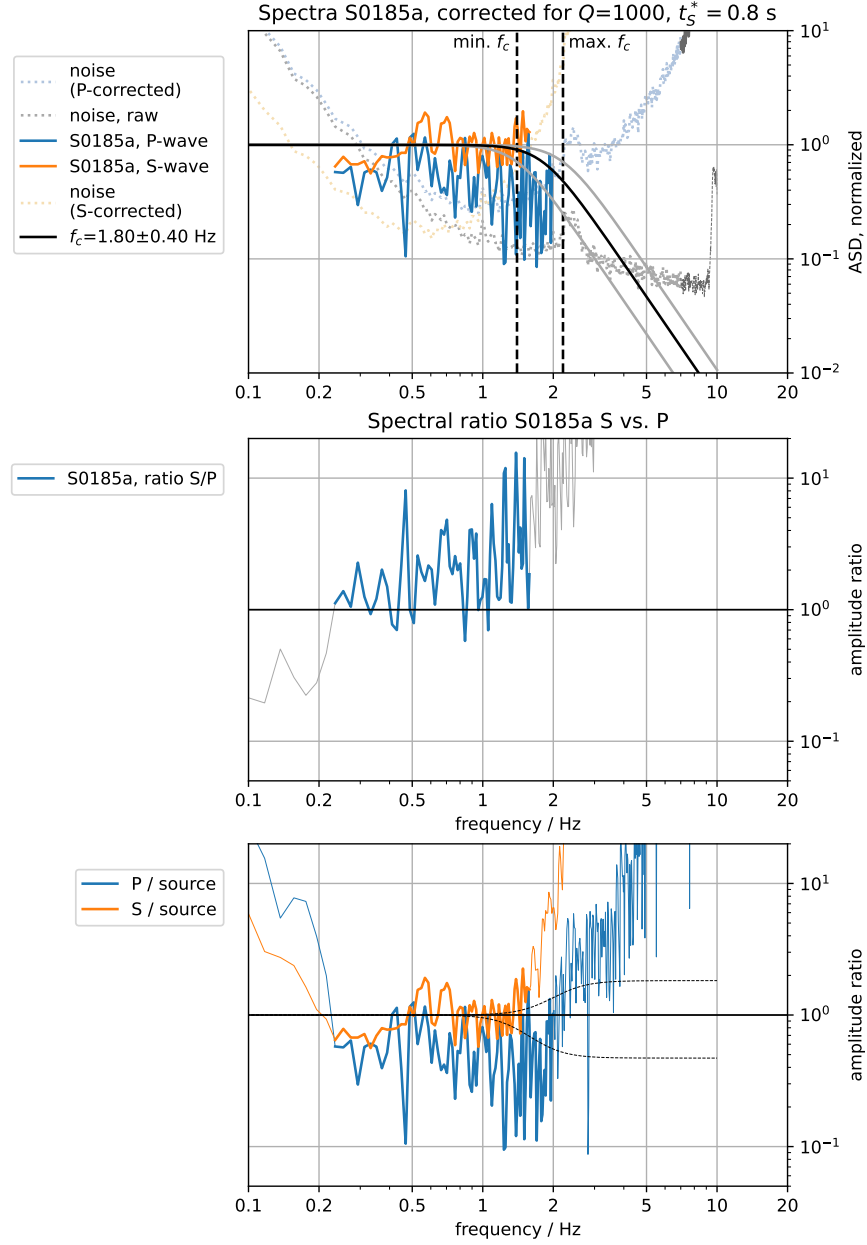


Figure 24: Event S0185aa, after correction for Q_μ (eq. 5, 6). Plot is otherwise identical to 14

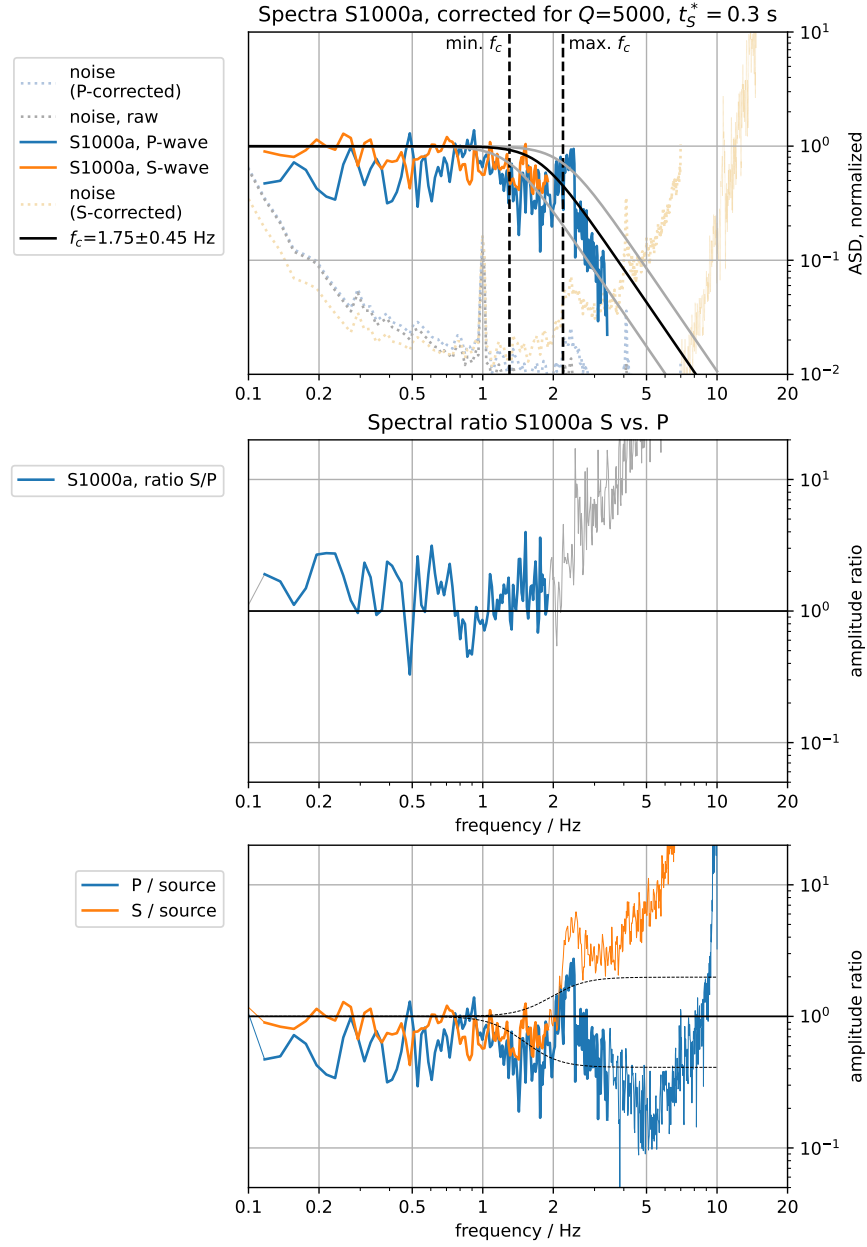


Figure 25: Event S1000a, after correction for Q_μ (eq. 5, 6). Plot is otherwise identical to 14

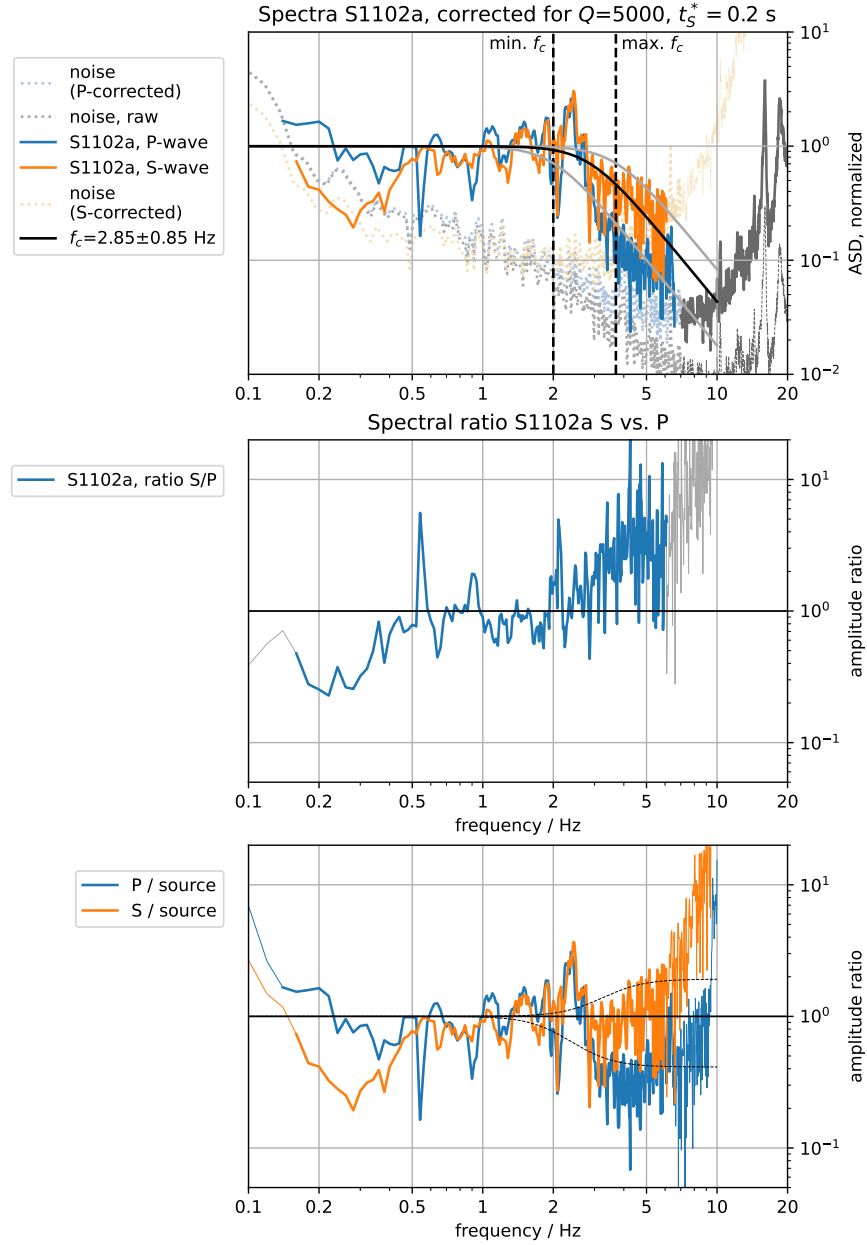


Figure 26: Event S1102a, after correction for Q_μ (eq. 5, 6). Plot is otherwise identical to 14